Meteorological conditions in a thinner Arctic sea ice regime from winter through summer during the Norwegian Young Sea Ice expedition (N-ICE2015)

Lana Cohen[1], Stephen R. Hudson[1], Von P. Walden[2], Robert M. Graham[1], Mats A. Granskog[1]

1. *Norwegian Polar Institute, Fram Centre, 9296 Tromsø, Norway*
2. *Washington State University, Department of Civil and Environmental Engineering, Pullman, Washington, USA.*

Corresponding author: Lana Cohen, email: Lana.Cohen@npolar.no

Draft: 15-February-2017

For submission to Journal of Geophysical Research – Atmospheres (N-ICE2015 special issue)

Keywords: N-ICE2015, Arctic, sea ice, Arctic meteorology, Arctic storms, atmospheric boundary layer, Arctic Oscillation, Arctic Dipole anomaly

Highlights:

- Analysis of a new comprehensive meteorological dataset over Arctic sea ice from winter to summer.
- Measurements of Arctic storms during winter show large but short-lived impact on atmospheric temperature.
- Spring/summer atmosphere is characterized by persistent temperature and humidity inversions indicative of clouds.

Abstract

Atmospheric measurements were made over Arctic sea ice north of Svalbard from winter through early summer (January—June) 2015 during the Norwegian Young Sea Ice (N-ICE2015) expedition. The dataset, which is available publicly, represents a comprehensive meteorological dataset covering the seasonal transition in the Arctic Basin over the new, thinner sea ice regime. Winter was characterized by a succession of storms that produced short-lived (less than 48 hours) temperature increases of 20 to 30 K at the surface. The storms were driven by the hemispheric-scale circulation pattern with a large meridional component of the polar jet stream steering North Atlantic storms into the high Arctic. Non-storm periods during winter were characterized by strong surface temperature inversions due to strong radiative cooling ('radiatively clear state'). The strength and depth of these inversions were similar to those during the SHEBA campaign. In contrast, atmospheric profiles during the 'opaquely cloudy state' were different to those from SHEBA due to differences in the synoptic conditions and location within the ice pack. Storm events observed during spring/summer were the result of synoptic systems located in the Barents Sea and the Arctic Basin, rather than passing directly over N-ICE2015. These synoptic systems were driven by a large-scale circulation pattern typical of recent years, with an Arctic Dipole pattern developing during June. Surface temperatures became near-constant 0˚C on 1 June marking the beginning of summer. Atmospheric profiles during the spring and early summer show persistent lifted temperature and moisture inversions that are indicative of clouds and cloud processes.

1. Introduction/Background

The Arctic is changing rapidly. Many studies have documented the decrease in sea ice extent and thickness, the lengthening of the melt season, and the increasing amount of open water that have been observed in recent decades [e.g., *Maslanik et al.,* 2007a; *Markus et al.,* 2009; *Maslanik et al.,* 2011; *Stroeve et al.,* 2012; *Vaughan et al.,* 2013; *Stroeve et al.,* 2014]. Much of the Arctic is now experiencing seasonal ice coverage and a greater portion of the ice pack is composed of first-year ice [*Nghiem et al.,* 2007; *Maslanik et al.,* 2011; *Comiso,* 2012]. These changes have been accompanied by considerable increases in Arctic surface air temperatures [*Overland et al.,* 2008], increased moisture fluxes [*Woods et al.,* 2013], changes in precipitation [*Screen and Simmonds*, 2012], as well as changes in the large-scale atmospheric circulation patterns [*Overland and Wang,* 2010; *Overland et al,* 2012]. One of the main processes driving 'Arctic Amplification' (i.e., greater warming in the Arctic than globally) is the sea ice albedo feedback [*Serreze and Barry,* 2011]. However, other processes have been shown to be important, especially increases in longwave radiation associated with moisture transport from lower latitudes [e.g., *Francis et al.,* 2005; *Graversen and Wang,* 2009; *Kapsch et al.,* 2014; *Park et al.,* 2015].

Several studies have shown that atmospheric circulation patterns can drive sea ice variability via various mechanisms such as changes to surface air temperatures (SAT) [e.g., *Graversen et al.,* 2011, *Yang et al.,* 2010] and sea surface temperatures (SST), shifts in wind patterns driving sea ice drift [e.g., *Ogi and Wallace,* 2012], and changes to storm tracks and storm activity [e.g., *Simmonds and Keay*, 2009; *Zhang et al.,* 2013]. Trends in atmospheric patterns such as the Arctic Oscillation and North Atlantic Oscillation have been linked to the variability in sea ice extent [e.g., *Stroeve et al.,* 2011; *Deser et al.,* 2000], and while these links do not explain the fundamental processes driving changes in the cryosphere, they can provide insights into the spatial and temporal variability of the changes. Significant shifts in the 'normal' large-scale atmospheric circulation pattern during summer months have been seen since 2005. In particular, a pattern known as the Arctic Dipole anomaly has emerged [*Overland et al.,* 2012]. This pattern has been suggested to have a causal relationship with record sea ice loss in 2007 [*Wang et al.,* 2009; *Lindsay et al.,* 2009], and it has been suggested that the Arctic may have entered a 'new state' of atmospheric variability [*X. Zhang et al.,* 2008; *Overland et al.,* 2008].

Storm characteristics (e.g., occurrence, tracks, intensity) are intricately related to the large-scale atmospheric circulation [*Simmonds et al.,* 2008], and storms in the Arctic have been suggested to have large impacts on sea ice [e.g., *Simmonds and Keay,* 2009; *Screen et al.,* 2011; *Boisvert et al.,* 2016]. These storms transport heat and moisture from lower latitudes, and the strong winds

associated with storms drive sea ice drift and upper-ocean mixing [*Peterson et al.,* 2017; *Meyer et al.,* this issue; *Itkin et al.,* this issue]. From an atmospheric viewpoint, the role of increased moisture convergence into the Arctic due to storms may be of most importance due to water vapor and cloud feedback effects on longwave radiation. Storms and synoptic activity bring clouds, which can have complicated impacts on the Arctic climate [e.g., *Kay et al,* 2008*; Perovich et al,* 2008*; J. Zhang et al,* 2008*; Schweiger et al.,* 2008; *Persson et al.,* 2016]. Clouds are an active area of research in the Arctic as they are one of the primary uncertainties in our understanding of Arctic amplification [e.g., *Sorteberg et al.,* 2005*; Liu et al.,* 2008*; Kay and Gettleman,* 2009]. Recent studies have shown that moisture transport associated with synoptic activity may explain some of the regional differences in changes in sea ice extent and concentration, such as the large variability in the Barents and Kara Seas [*Kapsch et al.,* 2014; *Park et al.,* 2015*; Woods and Caballero,* 2016].

The Arctic boundary layer is also of key importance for understanding the processes that drive sea ice variability. Quantifying fluxes of heat and moisture between the atmosphere and ice or ocean surface is necessary to quantify surface energy budgets over the Arctic, yet climate models have not been able to fully capture the temporal or spatial variability of surface heat fluxes over the Arctic [e.g., *Walsh et al.,* 2009*; Wyser et al.,* 2008; *Pithan et al.,* 2014; 2016]. Important positive feedback processes, such as the surface albedo feedback, water vapor feedback, and low-level cloud feedback, occur within the atmospheric boundary layer. Low-level clouds have been shown to drive much of the variability in the surface energy budget, as small changes in cloud cover and cloud properties can lead to relatively large changes in the surface energy budget [*Persson et al.,* 2002*; Intrieri et al.,* 2002]. Boundary layer properties in the Arctic are difficult to discern via satellite remote sensing. Moreover, boundary layer processes are different from those at mid-latitudes due to combination of high-latitude solar cycle and seasonal snow and ice cover. Therefore in-situ observations of the Arctic boundary layer are essential for understanding the rapidly changing Arctic and for linking the boundary layer processes to large-scale circulation patterns, which are more easily observed remotely.

Previous field experiments (e.g., CEAREX, AOE-01, ASCOS) have produced valuable measurements towards understanding Arctic sea ice-atmosphere interactions during the non-winter months [*CEAREX Drift Group,* 1990*; Tjernström* 2005*; Tjernström* 2014]. However, there are far fewer wintertime observations in the Arctic. The Soviet “North Pole” drifting stations made multiple year-round atmospheric measurements from 1954—1991, followed by the Russian North Pole drifting stations from 2003–2013 [*Kahl et al.,* 1999]. Following this, the Surface Heat Budget of the Arctic Ocean (SHEBA) experiment deployed a comprehensive suite of instrumentation to measure atmospheric, ice and ocean properties for a full year in 1997-1998 [*Uttal et al.,* 2002]. The

atmospheric observations made during SHEBA still represent an important observational dataset made during the Arctic winter [*Persson et al.,* 2016]. However the Arctic has changed considerably in the last two decades, and it is clear that the new, thinner sea ice regime is more susceptible to atmospheric forcing [*Maslanik et al.,* 2007a*; X. Zhang et al.,* 2008*; Lindsay et al.,* 2009]. Year-round observations of the physical processes occurring in the Arctic cryosphere are essential for testing and refining models, for developing and testing remote sensing observations, for assimilating into reanalyses products, and for providing basic information on the rapidly changing state of the Arctic [*Wyser et al.* 2008; *Pithan et al*., 2016]. Likewise, it is important to have such observations from a variety of regions in the Arctic, with different synoptic and sea ice conditions.

The Norwegian Young Sea Ice expedition (N-ICE2015) provides the first comprehensive set of winter measurements in a regime with younger and thinner sea ice that now dominates the Arctic. More information about the various components of the experiment is described in Granskog et al. (2016). This paper presents the meteorological measurements, with the goal of summarizing and characterizing the atmospheric conditions during the N-ICE2015 expedition (January—June 2015). This allows us both to put the accompanying results in context and to examine links between local and large-scale conditions. A brief description of the N-ICE2015 expedition and the atmospheric measurements are given in Section 2. Section 3.1 provides an overview of the meteorological conditions during N-ICE2015 from winter through early summer. Section 3.2 presents an analysis of the large-scale (Arctic-wide) atmospheric circulation patterns using reanalysis data, to put the meteorological data in context of Arctic-wide atmospheric situation. Sections 3.3 and 3.4 discuss the details of storm events and boundary layer conditions, providing some climatological context based on reanalysis datasets and comparisons to previous observations over Arctic sea ice (e.g., SHEBA). Finally, a summary and conclusions are given in Section 4.

2. Data

2.1 The N-ICE2015 expedition

The goal of N-ICE2015 was to improve our understanding of the current state of the Arctic sea ice system and the fundamental processes that are driving changes in the Arctic [*Granskog et al.,* 2016]. During N-ICE2015, observations of the atmosphere, ocean, ice dynamics, snow and ice physics, and marine ecosystem were made in the Atlantic sector of the Arctic Ocean north of Svalbard from mid-winter through early summer (Jan-Jun 2015). The Norwegian research vessel *Lance* was used as a research platform and was navigated into the ice pack north of Svalbard in early January 2015, moored to an ice floe, and drifted with the sea ice until it broke up. The break up of ice floes to the point where instruments could no longer be deployed on the ice happened three times, and each

time the ship was taken north again and instruments were redeployed on a new ice floe. A longer break was taken from mid-March to early-April to re-fuel and re-supply in Longyearbyen. The four drifts and their start and end dates are shown in Figure 1.

During each of the four drifts, *Lance* was moored to an ice floe and a science camp was established on the floe. The length of time at each floe was as follows: Floe 1 = 38 days, Floe 2 = 24 days, Floe 3 = 49 days, and Floe 4 = 16 days. Atmospheric measurements were made both from the ship and on the ice floe. The distance to the sea ice edge (> 15% sea ice concentration) was between 50 and 250 km for most of the experiment [*Itkin*, pers comm]. However, the sea ice in this region was very dynamic, and there were often open water leads nearby (within 1 km). The average location of the sea ice edge during N-ICE2015, which showed short-term variability but no significant seasonal changes, is shown in Figure 1. The general area for Floes 1 and 2 (Jan–Mar) was 81–83.5˚N, 16–28˚E and for Floes 3 and 4 (Apr–Jun) was 80–83.5˚N, 3–16˚E.

2.2 Atmospheric Measurements

2.2.1 Near-surface

Near-surface meteorological parameters were collected at the 'Supersite', which was established at each new floe 300 to 400 meters away from the ship to minimize interference from the ship, specifically with regards to heat and wind-shadowing. This site was the primary location for all off-ship atmospheric instrumentation. Figure 2a shows an aerial image of the Supersite and its relationship to the ship on Floe 3. At the Supersite, a 10-meter tower was installed 20 to 30 meters from a small power distribution hut. Temperature, humidity, and wind sensors (Table 1) were mounted on the tower approximately 2, 4 and 10 m above the snow surface (Figure 2b). The datalogger enclosure was mounted at the base of the tower and all sensor data was collected by the datalogger (Campbell Scientific CR3000) at 1 second resolution and averaged to 1 minute and 10 minute output files.

At the start of each drift, the Supersite was set up within a couple days after mooring to the new floe, and the meteorological sensors ran continuously until floe breakup cut the power source (Floes 1 & 2), felled the tower (Floe 2), and/or necessitated evacuation of the site (Floes 3 & 4). Shorter data gaps occurred in individual sensors due to cable problems, datalogger programming issues, or broken sensors. Ship-based measurements of temperature, pressure, and wind (Table 1) provide data to fill some of these data gaps, including times when the ship was moored to a floe but instruments at the Supersite were not yet installed. The ship-based instruments were mounted on the ship's mast approximately 22-24 m above the sea ice surface. The ship-based temperature and pressure data is not of the same quality as the Supersite measurements for several reasons including being more

directly influenced by the ship, the temperature sensor was not actively ventilated, and these instruments were not as well maintained as those at the Supersite. The ship-based wind sensor, mounted at ~24 m above ground level (agl), was used to reconstruct gaps in the 10 m wind data and is used in subsequent analysis; details of this reconstruction are described below in detail. The ship-based temperature and pressure were not used in any of the analyses, but provide an extended dataset for evaluating trends and other applications where high-accuracy measurements are not necessary. A summary of the instrumentation details and dates of operation is given in Table 1.

The pressure sensor (RM Young 61302V) was mounted inside the datalogger enclosure at the base of the tower with a port exposing it to the atmosphere. Temperature and relative humidity was measured with Vaisala HMP155 sensors mounted inside triple-walled actively aspirated radiation shields (RM Young Model 43502). The capacitive humidity sensor measures relative humidity directly and is calibrated with respect to liquid water (RH_w); measured values were then converted to relative humidity with respect to ice (RH_i) using the WMO standard [*World Meteorological Organization*, 2008].

Wind speed and direction were measured with 2D ultrasonic wind sensors (Lufft Ventus V200A-UMB), which were mounted at the end of arms ~1.5 m from the tower for the 2 and 4 m heights and mounted at the top of the tower for the 10 m height (Figure 2b). The sensors were heated to mitigate data losses due to transducer icing, and the sensors at 2 and 4 meters were never observed to have ice or frost on them (the 10 m sensor could not be visually inspected from the ground). Intermittent problems with the wind sensors during Floe 1 created considerable data gaps in the wind speed and direction datasets during this period (65% for 10 m height); these gaps were reconstructed using the ship-based wind data as described below. To correct the wind direction on rotating ice floes, wind directions were adjusted using *Lance's* navigation system. A daily direction 'offset' was calculated from the change in the ship's GPS-based navigation system. When the floes were rotating more quickly (e.g., at the late stages of Floe 2 and Floe 3, and all of Floe 4), the change in heading was calculated and applied at 3-hourly intervals.

Missing periods of data in the 10 m wind speed (indicated in Figure 3) were reconstructed from the ship-based wind sensor data (Thies Clima 2D ultrasonic), which was mounted at ~24 m. The wind profile power law was used to calculate wind speeds at 10 m using the 24 m wind speed values: $U_z = U_r * \left({}^{Z}/_{Z_r}\right)^{\alpha}$, where U_z is wind speed at height Z, U_r is wind speed at reference height (24 m), and α is an empirically derived value that depends on atmospheric stability. For all concurrent measurements of the 24 m and 10 m wind speeds (at 1-minute resolution), α was calculated as a function of U_r. The function for α can be approximated linearly within each of three wind regimes: U_r

≥ 10 m s^{-1}, 5 ≤ U_r < 10, and U_r < 5 m s^{-1}. Using α (U_r), winds were then calculated for the 10 m level. Comparing the measured 10 m wind speeds to the calculated 10 m wind speeds yields r = 0.97 and RMSE = 0.58 m s^{-1}, and the residual's mean and standard deviation is 0.07 and 0.88 m s^{-1} respectively. The reconstructed wind speeds account for 31% of the total dataset; most of these periods occur during Floe 1 (shown in Figure 3).

During Floes 1, 2, and 3, precipitation was collected in a Tretyakov shielded gauge, mounted 1–1.5 m above the surface and located 10 to 15 m from the meteorological tower. The contents of the gauge were collected daily at ~0700 UTC, melted (with lid on), and the water equivalent amount was measured to the nearest millimeter. Water volumes less than 1 mm were reported as 'trace'. Blowing snow and mixed solid/liquid precipitation events were also noted. One mm water equates to approximately 3 to 10 mm snow, depending on snow density. Measuring solid precipitation presents many challenges, and measurement biases are known to occur due to wetting losses, evaporation or sublimation, and wind undercatch. No corrections have been made for wetting loss errors as these are much less than the resolution of our measurements [*Goodison et al.,* 1998]. Wind undercatch is by far the most significant factor for errors in measuring solid precipitation. For Tretyakov shielded gauges, wind undercatch loss is on the order of 25 to 30% and can be up to 50% for high wind speeds (> 10 m s^{-1}) [*Goodison et al.,* 1998; *Rasmussen et al.,* 2012]. We have not corrected the measured precipitation values for wind conditions as the WMO undercatch corrections are only valid for wind speeds under 6 m s^{-1}, and Sugiura et al. (2006) show that, for these gauges, there is such considerable scatter in the undercatch ratio at higher wind speeds that extrapolating beyond 6 m s^{-1} is not appropriate.

2.2.2 Upper-air

Vertical profiles of temperature, relative humidity, and winds were measured from just above the surface to heights of up to 30 km using balloon-borne radiosondes [*Hudson et al.,* 2017; *Kayser et al.*, this issue]. The radiosondes were launched twice daily and coordinated with the WMO radiosonde network, with launches around 1100 and 2300 UTC to observe the atmosphere between 1100-1200 UTC and 2300-0000 UTC. Data from the sondes were transferred in near real-time to the Global Telecommunications System (GTS) data archive, to allow for incorporation into forecast models and reanalyses. Vaisala RS92-SGP sondes transmitted measurements back to the ship at 1-second resolution. Data were received, processed, and output with the Vaisala MW31 ground station. Ground checks were performed on each sonde to make sure that the sensors were functioning properly. Horizontal wind velocities and directions are derived from GPS measurements as the sonde moves with the winds. Heights above ground level have been calculated using pressure and

temperature. A total of 258 soundings were collected during the N-ICE2015 expedition between 16 January—26 March and 17 April—22 June.

3. Results and Discussion

3.1 Meteorology overview

For the N-ICE2015 meteorological data analysis, we define 'winter' as January—March (JFM), 'spring' as April—May (AM), and 'summer' as June for both physical and practical reasons. The month of March is more similar to winter than to spring in the high Arctic. For example, during N-ICE2015 the near-surface and upper atmospheric conditions are similar to those in mid-winter (December—February), incident sunlight remains near zero, and ocean dynamics, sea-ice, and biological systems remain generally unchanged from their winter states. This division between winter and spring also corresponds with the data gap between Floe 2 and Floe 3, which occurred from late March to early April. During April and May, the surface and atmosphere transitioned from spring conditions to summer conditions on 1 June. By 1 June, the near-surface temperature had risen to 0˚C and remained fixed near this value for the remainder of the experiment (Fig. 3b).

The full time-series of 1-minute resolution pressure (P), temperature (T), relative humidity (RH), wind speed, wind direction, and precipitation measurements [*Hudson et al.,* 2015] are shown in Figure 3. As described in Section 2, gaps in the time series are due to ice floe break-up and subsequent relocation to a new floe. The drift of each of the floes, and the dates they were occupied, are shown in Figure 1. The dates and details of the meteorological measurements are given in Table 1. Ship-based meteorological data is also shown in Figure 3, as discussed in Section 2. The ship-based wind speeds are adjusted to represent 10-m wind speeds. However, the ship-based temperature measurements and wind directions are unadjusted for height differences between the sensors. The ship-based temperature and pressure measurements are not used in any of the subsequent analysis.

Surface (sea-level) atmospheric pressure is shown in Figure 3a. The atmospheric pressure varied considerably during the winter, with rapid drops of over 30 hectopascals (hPa) occurring several times. The lowest pressure recorded was 965.4 hPa on 16 March. Surface pressure was less variable during the spring and summer compared with winter, and the mean pressure during spring and summer was higher than in winter (winter mean: 1000 hPa, spring mean: 1014 hPa). This is a reflection of the normal polar vortex weakening from winter to summer. The large pressure drops seen in winter are coincident with large increases in temperature, high wind speeds, and precipitation events and indicate the occurrence of synoptic-scale storm events in the region (Fig. 3).

Daily precipitation values are indicated in Figure 3a by blue stars. As discussed in section 2.2, these measurements may significantly underestimate actual precipitation values particularly during high winds. However, it is clear that all the precipitation events correspond to synoptic events during N-ICE2015, and that the larger storm events (as identified by pressure drops) produced more precipitation. The largest snowfall event was during the storm in early February, and produced a total of 20.3 mm water equivalent over five days (Figure 3a).

Near-surface air temperature (2 m) is shown in Figure 3b. During January and February, temperatures are mostly between -30 and -40˚C and similar low temperatures were experienced during non-storm periods in March. The lowest temperature recorded was -41.3˚C on 30 January. During winter, the most notable feature of the temperature is the large variability. There are several instances of rapid temperature rises, and subsequent decreases, of over 30 K over periods of a couple of days. In three of these cases the temperature increased over 20 K in less than 24 hours. Each of these warming events brought temperatures to near 0˚C. The storm events associated with these temperature variations are associated with transitions from the radiatively clear to the opaquely cloudy state [*Graham et al.,* 2016]. These storm events are discussed in greater detail in section 3.3 and by Graham et al. [2016], Kayser et al. [this issue] and Walden et al. [this issue].

Near-surface temperatures in spring show the normal seasonal rise in temperature. The highest recorded temperature was +1.7˚C on 15 June. With the exception of two temperature increases to just above 0˚C on 16 May and 19 May (which were both associated with a single storm), temperatures during spring do not rise above -10˚C until 24 May. The onset of summer, as seen from temperatures at near-constant 0˚C, is 1 June.

Meteorological data collected during the SHEBA experiment (October 1997 to October 1998) provides an opportunity to directly compare meteorological parameters collected over Arctic sea ice in winter [*Uttal et al.,* 2002; *Persson,* 2011]. Direct comparison with SHEBA is difficult as the SHEBA drift was located on the opposite side of the Arctic basin and further into the ice pack. However some Arctic-wide processes (e.g., boundary layer dynamics and cloud properties) are similar at both sites, and the differences illuminate regional variation and synoptic variability [*Graham et al.,* 2016].

Near-surface temperatures for SHEBA (1997-98) for the same winter period (JFM) show generally colder conditions with more frequent occurrence of -35 to -40˚C temperatures. Winter temperature variability during SHEBA was less extreme than during N-ICE2015. For example, the highest temperature in SHEBA from Jan—Mar was: -10˚C, compared with 0˚C during N-ICE2015. The warm events during SHEBA were also associated with the opaquely cloudy state. However, these were

much less intense than the storms experienced during N-ICE2015. This is demonstrated by the much lower surface pressures measured during the N-ICE2015 storm events (winter minimum: 965.4 hPa) as compared to SHEBA (winter minimum: 992.0 hPa) and summarized further by Graham et al., [2016, Table 1].

During the spring period, the range of N-ICE2015 surface pressure (999.7—1031.6 hPa) was similar to that during SHEBA (999.7—1038.4 hPa). From April to June, temperatures at SHEBA rose on similar timescales as during N-ICE2015, with the date of the onset of the summer melt season (as indicated by near-constant 0˚C temperatures) occurring at nearly the same time (29 May for SHEBA, 1 June for N-ICE2015). The onset of summer is also comparable to that reported from the Tara Expedition (April-Sept 2007). Tara drifted in a similar region of the Arctic as N-ICE2015, but was located further north (central drift location 87.6˚N, 63.8˚E). The onset of summer as defined for the Tara Expedition (mean diurnal temperatures above -1˚C) occurred on 9 June (2007) [*Vihma et al.,* 2008] and on 3 June for both N-ICE2015 and SHEBA using the same definition.

As with SHEBA, the amplitude of the mean diurnal temperature cycle during N-ICE2015 was largest during April and May and decreased significantly after the melt onset (1 June for N-ICE2015, 29 May for SHEBA) [*Persson et al.,*2002]. The mean diurnal amplitude for April (20-30 April) was 2˚C, for May was 1.8˚C, and for June (1-20 June) was 0.9˚C. The N-ICE2015 diurnal amplitudes are smaller than those for the same periods during SHEBA, which were 4.5˚C, 2.5˚C, and 1.4˚C respectively. This primarily reflects the larger mean downwelling shortwave radiation at SHEBA (mean diurnal maximums for April, May, and June periods were 100-150 W m^{-2} larger during SHEBA) [*Walden et al.,* this issue; *Persson,* 2011] as a result of SHEBA's lower latitude (central drift location Apr-June: 76.4˚N), but is likely also indicative of the different synoptic settings as discussed further in Section 3.3.

Near-surface (2 m) relative humidity with respect to ice (RH_i) during N-ICE2015 is plotted Figure 3c. During winter, conditions at the surface were always near saturation, or super-saturated, with respect to ice. This is corroborated by the frequent observations of ice fog and hoar frost during this period. In the spring, RH_i is more variable and is mostly sub-saturated, but remains above 80%. There were two short periods (20-22 April and 24 May) where RH_i drops below 80%. Both of these instances are likely due to dry polar air being advected into the region (based on NOAA-GFS surface pressure maps, not shown). The temporal variability of RH_i during N-ICE2015 is similar to that of SHEBA, where conditions remained mostly supersaturated until April, and then became more variable and near saturation (> 80%) [*Andreas et al.,* 2002].

Wind speed and wind direction (10 m) are shown in Figure 3d. These measurements include the 'reconstructed' 10 m winds from ship-based wind measurements as discussed in section 2.2.1. The highest wind speeds occurred during the storms in winter with the highest 1-minute wind speed recorded at 22.5 m s^{-1} on 15 February. Occurrences of strong winds during the winter period of N-ICE2015 are coincident with pressure drops and temperature increases due to storm events (Fig. 3). Wind rose plots for the winter and spring/summer periods are shown in Figure 4 and indicate a clear difference in the wind regimes for the different seasons. Winds during winter were more variable in both direction and speed with a higher occurrence of strong winds (> 10m s^{-1}) in winter (20% in JFM versus 10% in AMJ) but about equal occurrences of very low winds (< 2 m s^{-1}) (5% in JFM versus 6% in AMJ). The strongest winds during winter were east-southeasterly, but there was also a large occurrence of northwesterly strong winds. The strongest winds during AMJ were all northeasterly. These patterns are consistent with the differences in the storms that occurred during the two periods, and this is discussed further in section 3.3. Mean 10 m wind speeds during N-ICE2015 were considerably higher than those measured during SHEBA. SHEBA mean wind speeds for both the winter (JFM) and spring/summer (AMJ) periods was 4.9 m s^{-1} while for N-ICE2015 mean wind speeds were 6.8 m s^{-1} and 6.1 m s^{-1} for winter and spring/summer respectively.

Probability distributions of T, P, RH_i, and wind speed for both JFM and AMJ are shown in Figures 5a-h. The 2m temperature distributions (Figures 5b and 5f) show bimodal distributions in both seasons. For winter this is due to the distinct contrasts between the storm and non-storm periods related to the opaquely cloudy and radiatively clear states [*Graham et al.,* 2016; *Stramler et al.,* 2011]. In contrast, for spring and summer this bimodality represents the seasonal transition (e.g., 72% of temperatures ≥ -5˚C occur in June. Figures 5c and 5g also illustrate the differences between the winter and spring relative humidity with larger variability during spring and the near-constant saturated and super-saturated RH_i conditions during winter.

To put the N-ICE2015 observations into climatological context, Figures 5a-h include the mean distribution (dashed line) from the ECMWF ERA-Interim (ERA-I) reanalysis data [*Dee et al.,* 2011] from 1979-2015. ERA-I is used here as it has been shown to perform well in the Arctic when evaluated against in-situ data [*Lindsay et al.,* 2014]. The values used for the climatology are for the ERA-I grid-point corresponding to the central N-ICE2015 location for each season (JFM: 82˚N, 20.5˚E; AMJ: 81˚N, 12˚E). The full JFM (5a-d) and AMJ (5e-h) time periods were used to calculate the reanalysis distributions (i.e. the time periods are slightly longer than the corresponding N-ICE2015 time periods). The shaded region indicates the range of all ERA-I distributions for each season.

Figure 5a shows that N-ICE2015 experienced much higher frequencies of low pressures during the winter than the climatology indicating that the frequency of strong storms in this region was unusual. The observed wind speeds during winter (Figure 5d) also show a slight bimodal distribution which is likely indicative of the long calm periods that occurred between the passage of the storms and the high winds during the storms. The winter N-ICE2015 temperature distribution peak around -30˚C is primarily due to the frequent calm, cold periods experienced during surface temperature inversions (discussed further in Section 3.4). The peak winter temperature in the ERA-I climatology is much warmer compared with N-ICE2015 (Figure 5a). This is partly the result of a warm bias in ERA-I for cold and calm periods, likely due to the model's poor simulation of shallow surface inversions in the Arctic [*Tjernström and Graversen,* 2009; *Graham et al.,* 2016].

3.2 Large-scale atmospheric circulation during N-ICE2015

3.2.1 Arctic Oscillation and North Atlantic Oscillation

To place the local-scale meteorology in context with the synoptic scale, we use the NCEP Reanalysis datasets from NOAA/OAR/ESRL PSD (www.esrl.noaa.gov/psd/) [*Kalnay, et al.,* 1996] to analyze pressure (geopotential height), temperature, and wind patterns over the Arctic during the six month period of the N-ICE2015 expedition.

The winter period was characterized by an unusual atmospheric circulation pattern in the Northern Hemisphere, with a strong polar vortex centered over Greenland and northeastern Canada. This can be seen in the 500 hPa geopotential height (GPH) field in Figure 6a (solid contours). Figure 6a also shows the GPH anomaly from the climatological mean (1981-2010) in colored shading, which shows that the polar vortex was deeper (lower GPH) than normal and shifted over eastern North America. The cold air constrained by the polar air mass can be seen in the low-level air temperature anomalies (Figure 6b). During this period, eastern North America experienced colder than normal temperatures, while in western North America (and across the Arctic and Eurasia) temperatures were warmer than normal.

Because of the position of the polar air mass, the jet stream (which roughly follows the steepest gradient in 500 hPa GPH) in the North Atlantic sector of the Arctic during winter had an anomalous meridional component. This had the effect of steering North Atlantic-generated storms into the high-Arctic (north of 80˚N). This is reflected in the near-surface (925 hPa) anomaly wind vectors shown in Figure 6c. Southerly anomalies are evident in the Greenland and Norwegian Seas and persist as far north as Svalbard and the Barents Sea. Sea ice extent (SIE) in the Barents and Kara Seas was affected by the southerly winds, particularly the succession of storms that tracked into this region during February and March. The resulting low SIE in this region contributed strongly to the early occurrence

of the annual Arctic-wide maximum SIE. This was observed in late February 2015, rather than March, and moreover 2015 was the lowest maximum SIE in the 1979—2015 satellite record [*Perovich, et al.,* 2015].

The 2015 near-surface temperature and wind anomalies during spring/summer clearly contrast with the anomalies during winter (Figs 6e-f). These are indicative of the large scale circulation changes that occurred from winter to spring/summer. Figure 6d (contours) shows the seasonal weakening and expansion of the polar vortex over the central Arctic and Barents Seas, with more zonal flow across the Atlantic sector of the Arctic during spring/summer. The cold temperature anomalies in North America waned as the cold polar air shifted and warmed in AMJ. A significant positive temperature anomaly developed in spring/summer in the western Siberia/Kara Sea region (Fig 6e) associated with a southerly wind anomaly (Fig 6f). These winds were driven by the pressure gradient between a persistent high pressure anomaly over central Siberia and low pressure over northern Scandinavia (Fig 6d). In the region just south of N-ICE2015, between Greenland and Svalbard, near-surface wind anomalies shift from southerly in winter to northerly in spring/summer. In the N-ICE2015 region the warm temperature anomalies seen in winter (+3-4 K) are not seen in spring/summer where temperature anomalies are near zero (-1 to +1 K).

The Arctic Oscillation (AO) is the primary mode of Northern Hemispheric atmospheric variability and the AO index in large part describes the variability in strength of the polar vortex. Positive (negative) values of the AO index indicate a strong (weak) polar vortex. This means that the polar air mass is more (less) confined, and that the predominantly westerly winds that encircle the polar air mass are stronger (weaker) and located further poleward (equatorward). Variability in the AO has been linked to Arctic atmosphere and sea ice variability [*Rigor et al.,* 2002]. However recent studies have shown that since the 2000s, the AO is less well correlated with sea ice variability in the Arctic than the Arctic Dipole anomaly (discussed further below) [e.g., *Stroeve et al.,* 2012*; Overland et al.,* 2012].The AO index for the N-ICE2015 period is shown in Figure 7.

The North Atlantic Oscillation (NAO) index is also shown in Figure 7. The NAO can be considered the regional (North Atlantic) manifestation of the AO (Thompson and Wallace 1998). Both the NAO and AO indices were strongly positive in the winter of 2015, and more neutral for most of the second half of N-ICE2015 during spring. Both indices became negative in July after N-ICE2015. The NAO describes the pressure situation and strength of the westerlies in the North Atlantic. Positive AO/NAO is associated with more zonal jet structure while negative AO/NAO typically associated with more meridional components to the jet stream due to a more 'wavy' structure. However, during the 2015 winter, although the AO and NAO were positive, the jet stream in the Atlantic sector had a large

meridional component due to the position of the polar vortex being centered over Canada (Figure 6a). The anomalous northward-component of the jet stream in the Atlantic sector of the Arctic had the effect of driving cyclones generated in the North Atlantic northward into the high Arctic. In addition, the NAO and AO have been shown to have a strong relationship with cyclogenesis in the North Atlantic and Arctic, where positive AO/NAO indices correlate with more numerous and deeper cyclones [*Simmonds et al.,* 2008]. Thus, the succession of winter storms observed during N-ICE2015 were driven by the large-scale atmospheric conditions during this period.

The winter following N-ICE2015 (2015/2016) also experienced significant Arctic-wide warming and low sea ice anomalies driven by cyclonic activity. Recent studies have linked this to similar large-scale atmospheric conditions as N-ICE2015 (i.e. a northward component of the jet stream in the Atlantic sector of the Arctic) [*Boisvert et al.,* 2016; *Cullather et al.,* 2016; *Moore,* 2016; *Overland and Wang,* 2016]. Thus, understanding the N-ICE2015 winter large-scale conditions and links to synoptic variability are relevant to understanding changing Arctic conditions. Further analysis of the storms observed during N-ICE2015 is presented in Section 3.3.

3.2.2 Arctic Dipole Anomaly

During the spring and early summer, atmospheric circulation patterns shifted towards an Arctic Dipole (AD) pattern, with high pressure over the western Arctic and low pressure over the eastern Arctic. The surface wind fields that develop during an AD pattern have been linked to the sea ice minimums in 2007, 2010, and 2011 [e.g. *Stroeve et al.,* 2012*, Wang et al.,* 2009*; Lindsay et al,* 2009*, Ogi and Wallace,* 2012]. The AD pattern leads to a pressure gradient across the Arctic that drives winds across the Arctic basin from the Bering Sea to the Greenland and Barents Seas. This drives increased heat and moisture transport into the Arctic from the Pacific [*Graversen et al.,* 2011; *Kapsch et al.,* 2014], and increased ice export through the Fram Strait, as well as weakening of the Beaufort Gyre [*Wu et al.,* 2006*; Maslanik et al.,* 2007b*].* In addition to the wind forcing, the AD has been shown to influence sea ice variability through changes to the cloud cover and surface radiative balance [e.g., *Kay et al.,* 2008*, Schweiger et al.,* 2008*; Graversen et al.,* 2011*; Stroeve et al.,* 2012; *Kapsch et al.,* 2014].

We see evidence of a developing AD pattern in late May and June. The June 2015 sea level pressure fields (from NCEP reanalysis) in Figure 8a show lower pressures across eastern Arctic and higher pressures over much of the western Arctic. The pressure gradient between low pressure centered over the Barents Sea and the high pressure over Greenland produced near-surface (925 hPa) northerly wind anomalies in Atlantic sector (Figure 8c) which likely enhanced ice export during this period. On the eastern side of the Barents Sea low pressure, southerly wind anomalies (Figure 8c)

coincide with the warmest near-surface (925 hPa) temperature anomalies in the Arctic, as seen in Figure 8b.

There is a clear transition in the N-ICE2015 surface winds in late May that reflects the changes in the larger scale circulation. Measured 10 m winds at beginning of spring (18 Apr to 20 May) are lighter and more variable than winds later (20 May to 19 Jun), which were stronger and more northeasterly (Figure 3d). Both of these periods had the same number of storm events (described in section 3.3). For the first half of spring, the mean wind speed was 5.7 m s^{-1}, with wind speeds over 10 m s^{-1} only occurring 3.5% of the time; for the second half, the mean wind speed was 6.5 m s^{-1}, with wind speeds over 10 m s^{-1} occurring 16% of the time. Wind directions also changed between these two periods, with winds becoming more northeasterly during the second half (43% versus 61% of wind coming from the northeast sector (0-90˚)).

The changes in surface winds correspond to a significant reorganization of the Arctic atmospheric circulation pattern, which occurred from late May to early June. Daily 500 hPa geopotential height reanalysis maps (NCEP) (not shown) during this reorganization period show a persistent high pressure ridge over Western Canada/Alaska. This spreads across the Arctic and develops into upper-level ridging over Greenland in early June, with troughs developing both east and west of the ridge. The alternating regions of northward and southward flow anomalies over Canada and Greenland (yellow arrows in Figure 8c) are associated with the persistent ridging over Greenland caused by blocking events and may be indicative of a causal relationship for the AD [*Hanna et al.,* 2013*; Overland et al.,* 2012].

3.3 Synoptic Events

Synoptic-scale storms influence the cryosphere and ocean on both local and Arctic-wide scales. Individual storms are relatively transient events lasting on the order of 3-10 days, but storm occurrence, trajectories, and intensities are integrally related to the large-scale atmospheric circulation. Therefore, synoptic storms provide links between large-scale to local-scale effects that have been shown to directly influence Arctic SIE. Specifically, these events change the energy balance over large areas of the Arctic via heat and moisture advection, cloud radiative forcing, and turbulent mixing of the atmospheric boundary layer [e.g., *Graversen et al.,* 2008*; Sorteberg and Walsh,* 2008*; Screen et al.,* 2011; *Persson et al.*, 2016]. These events are also important for ocean and sea ice processes as drivers of mechanical sea ice disintegration [*Parkinson and Comiso,* 2013] and sea ice drift [*Comiso et al,* 2008*; Lindsay et al.,* 2009*, Ogi and Wallace,* 2012], precipitation [*Screen and Simmonds,* 2012], changes to sea surface temperatures (SST) [*Perovich et al,* 2008*; Steele et al,* 2008],

and changes to upper-level ocean mixing and structure [e.g., *Yang et al.,* 2004*; Zhang et al.,* 2013; *Meyer et al.,* this issue; *Peterson et al.,* 2017].

Table 2 provides a summary of the storms experienced during N-ICE2015. Storms are defined primarily by periods of strong winds and secondarily by decreases in atmospheric pressure. It is important to emphasize that the storm definitions used here are based only on the **local** conditions measured at the N-ICE2015 site so that they can be used in conjunction with other (multidisciplinary) N-ICE2015 observations. However, we show in the following analysis how the local characteristics correspond to the larger-scale synoptic conditions. The durations of the storms are defined by windiness, since this is the most influential feature of the storms that drives key parts of the ocean-sea ice system such as sea ice drift, snow distribution, ocean mixing, and turbulent heat fluxes. In particular, storms are defined as periods with 10-minute average wind speeds > 8 m s^{-1} that last for more than 3 hours, with no breaks longer than 1 hour. The intensity of the storms is characterized by the maximum rate of pressure decrease over a 6 hour period. Events that experienced a pressure decrease greater than 5 hPa in 6 hours are classified as 'Major' (M) storms, while those with a maximum rate of decrease less than 5 hPa in 6 hours are 'minor' (m) storms. This value is somewhat arbitrary. However, it correlates well with the duration of storms and other attributes listed in Table 2, such as peak wind speed, minimum pressure, and temperature increase during the storm. In general, the 'Major' storms experienced longer duration at N-ICE2015, stronger wind speeds, lower pressure and larger temperature increases than the minor storms. Peak wind speeds are based on the 1-minute average winds. To determine the pressure and temperature values, we use the period of one day before and after the strong wind period to capture the full range of pressure decreases and temperature increases.

3.3.1 Winter

As seen in Table 2, the most intense storms occurred during the winter. Six 'Major' storms were observed during the N-ICE2015 winter. Each 'Major' storm shows a considerable pressure decrease, large increase in temperature, high wind speeds, and precipitation (Figure 3). Storms M2, M3, and M6 were the most intense events, with pressures decreasing below 970 hPa, a decrease of over 60 hPa during M2 (1029 hPa to 967 hPa), peak sustained wind speeds around 20 m s^{-1}, and rapid temperature increases of greater than 30 K. All of the 'Major' winter storms brought near-melt temperatures to N-ICE2015 site and to large portions of the Arctic, particularly in the Atlantic sector, as seen in NOAA Global Forecast System (NOAA-GFS) maps (Figure 9).

Figure 9 shows the NOAA-GFS maps of sea level pressure (SLP) and surface temperature for each of the six 'Major' winter storms at the date/time (nearest 12-hourly interval) of lowest N-ICE2015-

measured pressure. The N-ICE2015 site is marked by an 'X' and black dots indicate the approximate center of the low pressure at daily intervals during the N-ICE2015-defined storm period and for 4 days prior. These storms clearly all show similar locations while impacting N-ICE2015 and have similar tracks travelling north into the Arctic via the Greenland Sea between Greenland and Svalbard. Storm M2 shows a particularly complex situation starting with a low pressure system travelling over the Greenland Ice Sheet and spinning off two smaller lows over northern Greenland (as noted by differently-shaded dots labeled '4-Feb' and '5-Feb'). A detailed analyses of this storm from radiosonde profiles is presented in Kayser et al. [this issue]. Storm M4 travelled more slowly than the other storms and is the only storm to track east of Iceland before entering the Greenland Sea.

The wind rose plots in Figure 4a and winds in Figure 3d corroborate the common pattern of the 'Major' storms. For each storm, they show strongest winds from the east-southeast and northwest. As the storm systems approached N-ICE2015 from the south, strong east-southeasterly winds occur, changing to northwesterly winds at the later stages of the storm passage. The shift in wind directions are associated with warm air advection and subsequent cold air advection, leading to the rapid warming and cooling seen in Figure 3 and in further detail in Kayser et al. [this issue] and for other Arctic storms in Persson et al. [2016]. The storms typically dissipated within two days of entering the high-Arctic. The three 'minor' storms (not shown) also tracked north up the Greenland Sea, but remained south of Svalbard before tracking east over the Barents Sea.

Previous studies indicate that the Greenland Sea is a common pathway for intense cyclones to enter the high-Arctic [*Tsukernik et al.,* 2007*; Sorteberg and Walsh,* 2008*; Simmonds et al.,* 2008]. Knowledge of whether the frequency and intensity of the storms during N-ICE2015 are unusual is important. Comparison of the winter surface pressure distribution measured during N-ICE2015 with that from the ERA-Interim climatology (1979-2015) in Figure 5 suggests that these storms were more frequent and/or more intense than normal [*Graham et al.,* 2016]. Preliminary work provides further evidence that these storms are exceptional in the climatological record (A. Rinke, personal communication 2017). This is the subject of future and on-going work.

3.3.2. Spring and Summer

The spring and summer storm events are less intense than the winter events, with smaller pressure drops, higher minimum pressures, and smaller temperature changes at the N-ICE2015 location (Table 2 and Figure 3). This follows the normal seasonal pattern of more intense and more frequent synoptic systems in the North Atlantic sector in winter, and less intense, more widely distributed systems in summer [*Serreze et al.,* 1997*; Zhang et al.,* 2004*; Sorteberg and Walsh,* 2008]. While less

intense than winter storms, spring and summer storms have been shown to be important drivers of sea ice variability [e.g., *Deser et al.,* 2000*; Screen et al.,* 2011*; Simmonds and Rudeva,* 2012].

Analyses of NOAA-GFS pressure maps (12 hourly) reveals that the synoptic settings for the N-ICE2015 spring storms was quite different than the winter storms (Figure 10). The depth and extent of the low pressures are smaller and none of the spring storms tracked directly over the N-ICE2015 study area. For most of the storms, the center of the storms tracks through the Barents and Kara Seas (m4, m5, m7, m8, m10, M7, M8) between 500-1500 km southeast of N-ICE2015. Figure 10a shows an example of the largest of one of these storms (M8) at the date/time of lowest pressure at the N-ICE2015 site (marked by the black X). The storm tracked northward into the central Arctic via the Barents and Kara Seas. Six other storms (listed above) also follow similar patterns, tracking south and east of Svalbard from the North Atlantic. The predominantly north and northeasterly winds generated by these storms' location in relation to N-ICE2015 are reflected in the wind rose plot (Figure 4b) and in the bottom panel of Figure 3.

Two other spring/summer storms (m6 and m9) had clearly different origins, impacting N-ICE2015 from the north after crossing the Arctic Basin. Figure 10b shows an example of one of these storms (m6) which was responsible for the strong temperature increases seen on both 16 and 19 May (Figure 3) as it tracked from the north over N-ICE2015 site (marked by black X).These two storms (m6 and m9) are clearly differentiated in the N-ICE2015 wind directions (Figure 3 and 4b) as they produced westerly and west-southwesterly winds rather than the northerly and northeasterlies produced by the other spring/summer storms.

Because the spring/summer storms did not track over the N-ICE2015 site like the winter storms, the distinction between 'Major' and 'minor' storms does not correlate as well with the larger synoptic-scale conditions as it does for winter. The storm with the lowest central pressure (based on NOAA-GFS) was M8 (lowest SLP ~975 hPa on 6 June). The other storms had lowest pressures between 980-1005 hPa. The wind speed and pressure drop during the event M7 was more related to a shifting high pressure to the west and northwest of the N-ICE2015 site rather than the low pressure system that was located more than 2000 km to the southeast.

Based on the comparison of spring/summer N-ICE2015 pressure distributions to the ERA-I climatology in Figure 5e, there was a slightly higher frequency of lower pressures during AMJ than is 'normal'. However whether this is directly related to the frequency of storms is unclear. The presence of an anomalous low pressure centered over the Barents Sea (Figure 6d and Figure 8a) during the end of May and into June likely had an influence on the pressure distribution. Figure 5h shows that the wind speed distribution during N-ICE2015 was the similar to the mean climatology.

To summarize, the spring and summer storm events are markedly different from the winter storms in terms of scale, intensity, and track, with weaker storms that did not pass directly over the N-ICE2015 site. This is largely due to the seasonal change as well as the differences in large-scale atmospheric circulation. While the winter large scale circulation was anomalous with a large meridional component in the North Atlantic which drove multiple storms into the high Arctic and over the N-ICE2015 site, the spring was impacted more by a persistent and anomalous low pressure centered over the Barents Sea .

3.4 Boundary Layer conditions during N-ICE2015

It is essential to understand boundary layer processes in the Arctic to understand the surface energy balance [see *Walden et al.,* this issue], particularly with respect to surface temperature response due to ice-albedo and cloud feedback processes. Boundary layer processes change significantly during the transition from winter to summer. During winter strong temperature inversions primarily develop due to strong radiative cooling and are strengthened by the advection of warm air from lower latitudes which overlay the colder air near the surface (e.g. *Tjernström et al.,* 2015). For the surface energy balance, temperature inversions can have significant negative feedback to surface cooling efficiency due to the re-radiation of near-surface warming being mostly directed back to the surface rather than out to space [*Bintanja et al.,* 2011]. The spring and summer boundary layer also has considerable impacts on surface energy balance with heat and moisture fluxes and cloud processes closely linked to boundary layer processes.

During the Arctic winter, the bimodal distribution of surface temperature has been shown to be indicative of a two-state atmosphere--clear and cloudy [e.g., *Graham et al,* this issue; *Stramler et al.,* 2011]. In terms of surface radiation balance, these states are very distinct: the cold periods coincide with clear, calm conditions that allow strong longwave radiative cooling, while the warm periods coincide with cloudy, stormy periods with high water vapor path and near zero net longwave fluxes at the surface [*Stramler et al.,* 2011; *Graham et al.,* this issue]. The cold, calm periods are also characterized by near-surface temperature inversions, where air temperature increases with height. This leads to a stably stratified boundary layer that is more isolated from the free troposphere and inhibits exchanges of heat, moisture, and trace gases from the free troposphere to the surface.

Winter radiosonde profiles (Figure 11) show the mean temperature profiles to 5 km above ground level (agl) for radiatively clear (Fig 11a) and opaquely cloudy states (Fig 11b). Identification of these two states are based on the bimodal distribution of net longwave (netLW) surface fluxes for the Arctic as shown by Stramler et al. (2011) and Graham et al., (this issue). For the radiatively clear state, netLW $<$ -30 W m^{-2} and for the opaquely cloudy state netLW $>$ -10 W m^{-2} . The figure shows

that surface temperature inversions over 5 K and 1000 m high are prevalent during the radiatively clear states (occurred in 61 of 107 winter profiles between 19 Jan to 17 Mar), while smaller (< 3 K) and shallower (~500 m) temperature inversions exist for the opaquely cloudy states (occurred in 44 of 107 winter profiles).

The same analysis is shown in Figure 11 for the SHEBA rawinsonde profiles [*Uttal et al.,* 2002; *Moritz,* 2017] for the same time periods as N-ICE2015 (19 Jan—17 Mar). The occurrences of radiatively clear (61 of 114 profiles) and opaquely cloudy (41 of 114) states are similar to N-ICE2015. The radiatively clear profiles are similar to N-ICE2015 with inversion heights around 1 km agl. Interestingly the SHEBA profiles show that the atmosphere was over 5 K warmer above the inversion than during N-ICE2015. This may be explained by the fact that a tightly constrained pool of cold polar air was located just west of the N-ICE2015 site during the winter of 2015, while during the winter of 1998, the polar vortex was not so tightly constrained (from NCEP reanalysis 500 hPa GPH analysis and AO index) and the region around the SHEBA site was influenced by a ridge of high pressure to the south.

For the opaquely cloudy cases, Figure 11b shows that SHEBA profiles below 2 km were very different than the N-ICE2015 profiles. While the N-ICE2015 profiles show small surface temperature inversions, SHEBA profiles indicate lifted temperature inversions between ~200-2000 m are common during cloudy conditions. These differences are likely indicative of the different synoptic settings that lead to these conditions, i.e. N-ICE2015 experienced more intense storms with stronger winds which lead to more mixing. It was also located closer to the sea ice edge, resulting in more heat and moisture being advected to the site during the opaquely cloudy conditions. There may also be differences in cloud properties, which is the focus of future study.

Temperature inversions at the surface are also identified by temperature gradients between 10 m and 2 m on the meteorological tower, which provide higher temporal resolution compared with the radiosondes. Temperature inversions occurred in this 10 m layer 80% of the time during the N-ICE2015 winter (mean $\Delta T = 0.7K$, maximum $\Delta T = 5.2K$), which is similar to conditions during the SHEBA experiment [*Persson et al.,* 2002]. For the same time period during SHEBA (15 Jan to 20 Mar, 1998), temperature inversions between 10 m and 2.5 m occurred 60% of the time (mean $\Delta T = 0.6K$, maximum $\Delta T = 5.3K$), indicating that these conditions are likely widespread and common during the Arctic winter. Other important characteristics of the Arctic boundary layer measured during N-ICE2015 (e.g., stability parameters and boundary layer heights) are discussed in further detail in Kayser et al., (this issue) and Walden et al., (this issue).

During the N-ICE2015 spring and summer, near-surface temperature inversions are not as common as the winter period. Figure 12 shows weekly averaged temperature profiles from radiosondes

between 12 April and 22 June (10 weeks). Surface inversions (as indicated by T increase from 0-100m agl) occurred in only 14 of 136 profiles during AMJ, of which 6 occurred in early spring (April 14-19th) and 6 in early summer (June 14 & 20-22). Slightly more of the surface temperature inversions (9 of 14) occurred during local 'night' (0000 UTC profiles, launched around 0100 local time) potentially indicating diurnal evolution of the boundary layer, as the sun was lower in the sky at night than during the day. A complete analyses of temperature inversions using the radiosonde dataset from N-ICE2015 is given by Kayser et al. [this issue]. The radiatively-driven diurnal cycle during spring and summer is discussed further in Walden et al. (this issue).

The weekly averaged profiles for spring and summer in Fig 12 show the seasonal warming of the atmosphere. The temperature profiles also show that a well-mixed layer often exists near the surface (i.e., temperature profiles follow adiabatic lapse rate near the surface) with one or more temperature inversions above ~500 m agl. These features are persistent as indicated by the fact that they are seen in the weekly averaged profiles. These features have also been shown to be common throughout the high Arctic in summer months [e.g., *Intrieri et al.,* 2002*; Tjernström et al.,* 2012*; Nygård et al.,* 2014] and are indicative of the prevalence of low-layer cloud in the Arctic during spring and summer.

Temperature inversions are mostly co-located with specific humidity (q) inversions during spring and summer. Only 3 of 136 soundings from the spring / summer period of N-ICE2015 do not have at least one co-located T and q inversion, and many profiles display multiple inversion layers. The collocated temperature and specific humidity inversions are indicative of cloud-top processes [*Sedlar and Tjernström,* 2009*; Sedlar et al.,* 2012], and this is supported by the N-ICE2015 profiles where they often occur at the top of saturated layers (RH_i > 100%) as seen in Figure 13, which shows an example profile from 6 May (launched ~23 UTC). Frequency distribution of the heights of the collocated T and q inversions during spring and summer give three distinct peaks at ~500 m agl (13.5% between 450-550m), at ~1400 (3.3%), and ~2400 m (1.4%). Low-level clouds and relative humidity in the boundary layer play a significant role in the surface energy balance of the Arctic [*Andreas et al.,* 2002] and further study of cloud properties and the radiative effects of clouds from ceilometer and lidar measurements made during N-ICE2015 is the subject of future and on-going work.

4. Conclusions

Atmospheric measurements made during the N-ICE2015 expedition [*Hudson et al.,* 2015] provide a unique dataset from winter through spring in the North Atlantic Sector of the Arctic, a key region for understanding Arctic sea ice. During the winter period of N-ICE2015 (January-March 2015), the jet stream had an anomalously large meridional component that drove several intense storms into the

high Arctic (north of 80˚N), passing over the N-ICE2015 study area. These winter storms had a considerable, but relatively short-lived, effect on the heat budget as seen in large temperature increases to near 0˚C, with rapid return to cold, stably stratified conditions after each storm passed.

The N-ICE2015 meteorological data show that the non-storm periods in the winter are characterized by strong surface temperature inversions. Comparisons of atmospheric profiles from radiosondes for the radiatively clear state show very similar structures to the boundary layer structures for both N-ICE2015 and SHEBA. Similarly, measurements from the meteorological tower show similar frequency of occurrence of inversions near the surface (lowest 10 m) for the two campaigns. However, comparison of the opaquely cloudy state show marked differences to SHEBA data. Opaquely cloudy states during N-ICE2015 have a very shallow or no surface temperature inversion, whereas SHEBA shows lifted inversions are very common for the opaquely cloudy state from near-surface to ~2km. The atmospheric measurements during N-ICE2015 which capture both clear and cloudy states in the Arctic winter and the transitions between are unique. Further investigation of the changes to the atmospheric boundary layer structure and surface energy balance during these transitions are discussed further in Walden et al., (this issue), Graham et al., (this issue) and Kayser et al. (this issue).

The strong winds associated with the storms observed during N-ICE2015 have important impacts on Arctic sea ice and ocean. These winds have been shown to drive upper-ocean mixing [*Meyer et al.,* this issue] and can increase ocean-to-ice heat fluxes [*Peterson et al.,* 2017]. Storms are also shown to affect sea ice deformation especially in a thinner sea ice regime [*Itkin et al.,* this issue] and these deformation events resulted in snow-ice formation [*Provost et al.,* this issue]. Indirectly, the more dynamic ice pack following storms can result in more open water (leads) that support under-ice phytoplankton blooms further north and earlier in the season than previously experienced in the Arctic [*Assmy et al.,* 2017].

The spring period during N-ICE2015 (18 April-19 June) reveals very different meteorological conditions to those observed during winter. The intense storms that were driven into the high Arctic from the North Atlantic during the winter period did not occur during spring and summer. Instead, the storm events during spring/summer which impacted N-ICE2015 were due to smaller, less intense low pressures, mostly centered in the Barents Sea over 500 km from the N-ICE2015 study area. The large scale circulation during spring and summer included the development of an Arctic Dipole pattern in June and the influence of a low pressure anomaly centered in the Barents Sea.

The time series of near-surface temperature from N-ICE2015 show ‘summer’ beginning around the first week of June. This timing is similar to previous Arctic campaigns such as SHEBA and Tara.

Atmospheric profiles show that the near-surface during spring/summer is very well mixed, but one or more temperature and specific humidity inversions above ~200 m are present almost constantly. These conditions are associated with and intricately linked to the existence of clouds and cloud formation processes. Cloud properties are extremely important in determining surface energy balance and are the subject of future studies.

Acknowledgements

This work has been supported by the Norwegian Polar Institute's Centre for Ice, Climate and Ecosystems (ICE) through the N-ICE project. We would like to thank all members of the N-ICE2015 team and the crew of R/V Lance for their help collecting and producing the N-ICE2015 dataset. The N-ICE2015 radiosonde program was also supported by the Alfred Wegener Institute and Korean Polar Research Institute. V.P. Walden acknowledges support from the U.S-Norway Fulbright Distinguished Arctic Chair Program and Washington State University. We gratefully acknowledge use of the NOAA CPC-NCEP Global Forecast System data available at: www.ncdc.noaa.gov/data-access/model-data/model-datasets/global-forcast-system-gfs. The SHEBA data are provided by NCAR/EOL under sponsorship of the National Science Foundation, http://data.eol.ucar.edu/. The N-ICE2015 data are available through the Norwegian Polar Data Centre: https://data.npolar.no. We acknowledge the use of open-source software sponsored by NumFocus (http://www.numfocus.org) in our data analysis, including Interactive Python (ipython) [*Perez and Granger,* 2007] and matplotlib [*Hunter,* 2007]. We also gratefully acknowledge the constructive comments on this manuscript from three anonymous reviewers.

References

Andreas, E. L., P. S. Guest, P. O. G. Persson, C. W. Fairall, T. W. Horst, S. R. Semmer, and R. E. Moritz (2002), Near-surface water vapor over polar sea ice is always near ice saturation, *J. Geophys. Res.,* 107(C10), doi:10.1029/2000JC000411.

Assmy, P., and 39 others (2017), Leads in Arctic pack ice enable early phytoplankton blooms below snow-covered sea ice, *Scientific Reports*, 7, 40850, doi:10.1038/srep40850.

Bintanja, R., R. Graversen, and W. Hazeleger (2011), Arctic winter warming amplified by the thermal inversion and consequent low infrared cooling to space. *Nat. Geosci.,* 4, 758–761, doi: 10.1038/ngeo1285.

Boisvert, L. N., A. A. Petty, and J. C. Stroeve (2016), The Impact of the Extreme Winter 2015/16 Arctic Cyclone on the Barents–Kara Seas, *Mon. Weather Rev.*, *144*(11), 4279–4287, doi:10.1175/MWR-D-16-0234.1.

CEAREX Drift Group (1990), CEAREX Drift Experiment, *Eos Trans. AGU*, 71(40), 1115–1118, doi: 10.1029/90EO00311.

Comiso, J. C., C. L. Parkinson, R. Gersten, and L. Stock (2008), Accelerated decline in the Arctic sea ice cover, *Geophys. Res. Lett*., 35, L01703, doi: 10.1029/2007GL031972.

Comiso, J.C. (2012) Large Decadal Decline of the Arctic Multiyear Ice Cover. *J. Climate,* 25, 1176–1193, doi: 10.1175/JCLI-D-11-00113.1.

Cullather, R. I., Y. Lim, L. N. Boisvert, L. Brucker, J. N. Lee, and S. M. J. Nowicki (2016), Analysis of the warmest Arctic winter, 2015-2016, *Geophys. Res. Lett.*, 808–816, doi:10.1002/2016GL071228.

Dee, D. P., et al. (2011), The ERA-Interim reanalysis: Configuration and performance of the data assimilation system, *Q. J. R. Meteorol. Soc.*, *137*(656), 553–597, doi:10.1002/qj.828.

Deser, C., J.E. Walsh, M.S. Timlin (2000), Arctic sea ice variability in the context of recent atmospheric circulation trends*, J. Climate,* 13, 617-633.

Francis, J. A., E. Hunter, J. R. Key, and X. Wang (2005), Clues to variability in Arctic minimum sea ice extent, *Geophys. Res. Lett.,* 32, L21501, doi: 10.1029/2005GL024376.

Goodison, P. Y. T. Louie, and D. Yang (1998), WMO solid precipitation measurement intercomparison. WMO Instruments and Observing Methods Rep. 67, WMO/TD-872, 212 pp.

Graham, R. M., A. Rinke, L. Cohen, S. R. Hudson, V. P. Walden, M. A. Granskog, W. Dorn, M. Kayser, M. Maturilli (2016), A comparison of the two Arctic atmospheric winter states during the N-ICE2015 and SHEBA campaigns, *J. Geophys. Res. Atmos*., doi: 10.1002/2016JD025475

Granskog, M. A., P. Assmy, S. Gerland, G. Spreen, H. Steen, and L. H. Smedsrud (2016), Arctic research on thin ice: Consequences of Arctic sea ice loss, *Eos,* 97, doi:10.1029/2016EO044097.

Graversen, R. G., T. Mauritsen, M. Tjernström, E. Källen, G. Svensson (2008), Vertical structure of recent Arctic warming, *Nature*, 451, 53-56, doi: 10.1038/nature06502.

Graversen, R. G., T. Mauritsen, S. Drijfhout, M. Tjernström, and S. Mårtensson (2011), Warm winds from the Pacific caused extensive Arctic sea-ice melt in summer 2007, *Clim. Dyn.,* 36:2103, doi:10.1007/s00382-010-0809-z.

Graversen, R.G. and M. Wang, (2009) Polar amplification in a coupled climate model with locked albedo, *Clim. Dyn.,* 33:629, doi:10.1007/s00382-009-0535-6.

Hanna, E., Jones, J. M., Cappelen, J., Mernild, S. H., Wood, L., Steffen, K. and Huybrechts, P. (2013), The influence of North Atlantic atmospheric and oceanic forcing effects on 1900–2010 Greenland summer climate and ice melt/runoff, *Int. J. Climatol.,* 33: 862–880. doi:10.1002/joc.3475.

Hudson, S. R., L. Cohen, and V. Walden, (2015) N-ICE2015 surface meteorology [Data set]. Norwegian Polar Institute. https://doi.org/10.21334/npolar.2015.056a61d1.

Hudson, S., L. Cohen, M. Kayser, M. Maturilli, J.H. Kim, S. J. Park, W. Moon, M. A. Granskog (2017), N-ICE2015 atmospheric profiles from radiosondes. Norwegian Polar Institute, Alfred Wegener Institute, Korean Polar Research Institute, https://data.npolar.no/dataset/216df9b3-e2bd-5111-9c02-fea848d76670.

Hunter, J.D. (2007), Matplotlib: A 2D graphics environment, *Computing in Science & Engineering,* 9(3): 90-95.

Itkin, P., G. Spreen, B. Cheng, M. Doble, F. Girard-Ardhuin, J. Haapala, S. R. Hudson, N. Hughes, L. Kaleschke, M. Nicolaus, J. Wilkinson (this issue), Thin ice and storms: a case study of sea ice deformation from buoy arrays deployed during N-ICE2015, *J. Geophys. Res.Oceans*

Kahl, J.D.W., N. A. Zaitseva, V. Khattatov, R. C. Schnell, D. M. Bacon, J. Bacon, V. Radionov, and M. C. Serreze (1999), Radiosonde Observations from the Former Soviet "North Pole" Series of Drifting Ice Stations, 1954–90, *Bull. Amer. Meteor. Soc.,* 80, 2019–2026.

Kalnay, E., Kanamitsu, M., Kistler, et al., (1996), The NCEP/NCAR 40-Year Reanalysis Project, *B. Am. Meteorol. Soc.,* 77, 437–470.

Kapsch, M. L., R. G. Graversen, T. Economou, and M. Tjernström (2014), The importance of spring atmospheric conditions for predictions of the Arctic summer sea ice extent, *Geophys. Res. Lett.,* 41, 5288–5296, doi:10.1002/2014GL060826.

Kay J.E., L'Ecuyer T., Gettelman A., Stephens G., O'Dell C. (2008), The contribution of cloud and radiation anomalies to the 2007 Arctic sea ice extent minimum, *Geophys. Res. Lett.,* 35, L08503, doi: 10.1029/2008GL033451.

Kay, J. E., and A. Gettelman (2009), Cloud influence on and response to seasonal Arctic sea ice loss, *J. Geophys. Res*., 114, D18204, doi: 10.1029/2009JD011773.

Kayser, M., M. Maturilli, L. Cohen, S. R. Hudson, R. Graham, A. Rinke, M. A. Granskog (this issue), Climatological context and regional representativeness of upper-air observations during the Norwegian Young Sea ICE expedition (N-ICE2015). *J. Geophys. Res. Atmos.*

Lindsay, R. W., J. Zhang, A. Schweiger, M. Steele, and H. Stern (2009), Arctic sea ice retreat in 2007 follows thinning trend, *J. Climate,* 22, 165–176, doi: 10.1175/2008JCLI2521.1.

Lindsay, R., M. Wensnahan, A. Schweiger, and J. Zhang (2014), Evaluation of Seven Different Atmospheric Reanalysis Products in the Arctic. *J. Climate,* **27**, 2588–2606,doi: 10.1175/JCLI-D-13-00014.1.

Liu, Y., J. R. Key, and X. Wang (2008), The influence of changes in cloud cover on recent surface temperature trends in the Arctic, *J. Clim.,* 21, 705-715.

Maslanik, J. A., C. Fowler, J. Stroeve, S. Drobot, J. Zwally, D. Yi, and W. Emery (2007a,) A younger, thinner Arctic ice cover: Increased potential for rapid, extensive sea-ice loss, *Geophys. Res. Lett.*, 34, L24501, doi: 10.1029/2007GL032043.

Maslanik, J., S. Drobot, C. Fowler, W. Emery, and R. Barry (2007b), On the Arctic climate paradox and the continuing role of atmospheric circulation in affecting sea ice conditions*, Geophys. Res. Lett.,* 34, L03711, doi:10.1029/2006GL028269.

Maslanik, J., J. Stroeve, C. Fowler, and W. Emery 2011, Distribution and trends in Arctic sea ice age through spring 2011. *Geophys. Res. Lett.* 38, L13502, doi:10.1029/2011GL047735.

Markus, T., J. C. Stroeve, and J. Miller (2009), Recent changes in Arctic sea ice melt onset, freezeup, and melt season length, *J. Geophys. Res*., 114, C12024, doi:10.1029/2009JC005436.

Meyer, A., I. Fer, A. Sundfjord, (this issue) Mixing rates and vertical heat fluxes north of Svalbard from Arctic winter to spring, *J. Geophys. Res. Oceans,*

Moore, G. W. K. (2016), The December 2015 North Pole Warming Event and the Increasing Occurrence of Such Events, *Sci. Rep.*, *6*(November), 39084, doi:10.1038/srep39084.

Moritz, R. (2017), Soundings, Ice Camp NCAR/GLAS raobs. (ASCII). Version 2.0. UCAR/NCAR - Earth Observing Laboratory. https://doi.org/10.5065/D6FQ9V0Z.

Nghiem S. V., I. G. Rigor, D. K. Perovich, P. Clemente-Colon, J. W. Weatherly, G. Neumann (2007), Rapid reduction of Arctic perennial sea ice. *Geophys. Res. Lett*., 34, L19504, doi: 10.1029/2007GL031138.

Nygård T., T. Valkonen, T. Vihma (2014), Characteristics of Arctic low-tropospheric humidity inversions based on radio soundings, *Atmos. Chem. Phys*., 14, 1959-1971, doi: 10.5194/acp-14-1959-2014.

Ogi, M., and J. M. Wallace (2012), The role of summer surface wind anomalies in the summer Arctic sea ice extent in 2010 and 2011, *Geophys. Res. Lett.,* 39, L09704, doi:10.1029/2012GL051330.

Overland, J. E., M. Wang, and S. Salo (2008), The recent arctic warm period, *Tellus A*, 60(4), 589-597.

Overland J.E. and Wang, M. (2010), Large-scale atmospheric circulation changes associated with the recent loss of Arctic sea ice, *Tellus,* 62A:1-9.

Overland, J. E., and M. Wang (2016), Recent Extreme Arctic Temperatures are due to a Split Polar Vortex, *J. Climate*, *29*(15), 5609–5616, doi:10.1175/JCLI-D-16-0320.1.

Overland J.E., J. A. Francis, E. Hanna, M. Wang, (2012), The recent shift in early summer Arctic atmospheric circulation, *Geophys. Res. Lett.,* 39:L19804.

Park, H.-S., S. Lee, S.-W. Son, S. B. Feldstein, and Y. Kosaka, (2015), The impact of poleward moisture and sensible heat flux on Arctic winter sea ice variability, *J. Climate*, 28, 5030–5040, doi:10.1175/JCLI-D-15-0074.1.

Parkinson, C. L., and J. C. Comiso (2013), On the 2012 record low Arctic sea ice cover: Combined impact of preconditioning and an August storm, *Geophys. Res. Lett.*, 40, 1356–1361, doi:10.1002/grl.50349.

Pérez, F. and B.E. Granger, *IPython: A System for Interactive Scientific Computing*, Computing in Science and Engineering, vol. 9, no. 3, pp. 21-29, May/June 2007, doi:10.1109/MCSE.2007.53.

Perovich, D. K., J. A. Richter-Menge, K. F. Jones, and B. Light (2008), Sunlight, water, and ice: Extreme Arctic sea ice melt during the summer of 2007, *Geophys. Res. Lett.*, 35, L11501, doi:10.1029/2008GL034007.

Perovich, D., W. Meier, M. Tschudi, S. Farrell, S. Gerland, S. Hendricks (2015), Arctic Report Card: Update for 2015, Sea Ice, http://www.arctic.noaa.gov/reportcard/sea_ice.html, Dec 15, 2015.

Persson, P. O. G., C. W. Fairall, E. L. Andreas, P. S. Guest, and D. K. Perovich (2002), Measurements near the Atmospheric Surface Flux Group tower at SHEBA: Near-surface conditions and surface energy budget, *J. Geophys. Res.,* 107(C10), 8045, doi:10.1029/2000JC000705.

Persson, O. (2011), SHEBA Composite Data Observations. Version 1.0. UCAR/NCAR - Earth Observing Laboratory. https://doi.org/10.5065/D6PN93R6. Accessed 24 Jan 2017.

Persson, P. O. G., M. D. Shupe, D. Perovich, A. Solomon (2016) Linking atmospheric synoptic transport, cloud phase, surface energy fluxes, and sea-ice growth: observations of midwinter SHEBA conditions, *Clim Dyn.*, doi:10.1007/s00382-016-3383-1.

Peterson, A. K., I. Fer, M. G. McPhee, A. Randelhoff (2017), Turbulent heat and momentum fluxes in the upper ocean under Arctic sea ice*. J. Geophys. Res.,* doi: 10.1002/2016JC012283.

Pithan, F., B. Medeiros, and T. Mauritsen (2014), Mixed-phase clouds cause climate model biases in Arctic wintertime temperature inversions, *Clim. Dyn.*, *43*(1-2), 289–303, doi:10.1007/s00382-013-1964-9.

Pithan, F., et al. (2016), Select strengths and biases of models in representing the Arctic winter boundary layer over sea ice: the Larcform 1 single column model intercomparison, *J. Adv. Model. Earth Syst.,* 8, doi:10.1002/2016MS000630.

Provost, C., N. Sennéchael, J. Miguet, P. Itkin, A. Rösel, Z. Koenig, N. Villacieros and M. A. Granskog (this issue), Observations of snow-ice formation in a thinner Arctic sea ice regime during the N-ICE2015 campaign: influence of basal ice melt and storms. *J. Geophys. Res. Oceans*,

Rasmussen, R., et al., (2012), How well are we measuring snow? *Bull. Amer. Meteor. Soc.,* 93, 811-829, doi: 10.1175/BAMS-D-11-00052.1.

Rigor, I. G., J. M. Wallace, R. L. Colony (2002), Response of sea ice to the Arctic Oscillation*. J. Climate,* **15**, 2648–2663.

Screen, J. A., I. Simmonds, and K. Keay (2011), Dramatic interannual changes of perennial Arctic sea ice linked to abnormal summer storm activity, *J. Geophys. Res.,* 116, D15105, doi: 10.1029/2011JD015847.

Screen, J. A., and I. Simmonds (2012), Declining summer snowfall in the Arctic: Causes, impacts and feedbacks, *Clim. Dyn.,* 38, 2243–2256, doi:10.1007/s00382-011-1105-2.

Sedlar, J. and Tjernström, M. (2009), Stratiform Cloud-Inversion Characterization During the Arctic Melt Season, *Bound.-Lay. Meterol.*, 132, 455–474, doi:10.1007/s10546-009-9407-1.

Sedlar, J., Shupe, M. D., and Tjernström, M. (2012), On the Relationship between Thermodynamic Structure and Cloud Top, and its Climate Significance in the Arctic, *J. Climate,* 25, 2374–2393, doi:10.1175/jcli-d-11-00186.1.

Serreze, M., F. Carse, R. G. Barry, J. C. Rogers (1997), Icelandic Low cyclone activity: Climatological features, linkages with the NAO and relationships with recent changes in the Northern Hemisphere circulation, *J. Climate,* 10, 453-464.

Serreze, M. C. and R.G. Barry (2011) Processes and impacts of arctic amplification: A research synthesis, *Global Planet. Change,* 77, 85-96.

Simmonds, I., C. Burke, K., Keay (2008), Arctic climate change as manifest in cyclone behavior, *J. Climate*, 21, 5777-5796, doi: 10.1175/2008JCLI2366.1.

Simmonds, I., and K. Keay (2009), Extraordinary September Arctic sea ice reductions and their relationships with storm behavior over 1979–2008, *Geophys. Res. Lett.,* 36, L19715, doi: 10.1029/2009GL039810.

Simmonds, I., and I. Rudeva (2012), The great Arctic cyclone of August 2012, *Geophys. Res. Lett.,* 39, L23709, doi: 10.1029/2012GL054259.

Sorteberg A., T. Furevik, H. Drange, and N. G. Kvamstø (2005) Effects of simulated natural variability on Arctic temperature projections, *Geophys. Res. Lett.,* 32, L18708, doi: 10.1029/2005GL023404.

Sorteberg, A. and J. E. Walsh (2008) Seasonal cyclone variability at 70N and its impact on moisture transport into the Arctic, *Tellus,* 60A, 570-586.

Stramler, K., A. D. Del Genio, and W. B. Rossow (2011), Synoptically driven Arctic winter states, *J. Climate*, *24*(6), 1747–1762, doi:10.1175/2010JCLI3817.1

Steele, M., W. Ermold, and J. Zhang (2008), Arctic Ocean surface warming trends over the past 100 years, *Geophys. Res. Lett.,* 35, L02614, doi: 10.1029/2007GL031651.

Stroeve J. C., J. Maslanik, M. C. Serreze, I. Rigor, W. Meier (2011), Sea ice response to an extreme negative phase of the Arctic Oscillation during winter 2009/2010, *Geophys Res Lett.* doi: 10.1029/2010GL045662.

Stroeve, J. C., M. C. Serreze, M. M. Holland, J. E. Kay, J. Maslanik, and A. P. Barrett (2012), The Arctic's rapidly shrinking sea ice cover: A research synthesis, *Clim. Change,* 110, 1005–1027, doi:10.1007/s10584-011-0101-1.

Stroeve, J. C., T. Mark us, L. Boisvert, J. Miller, and A. Barrett (2014), Changes in Arctic melt season and implications for sea ice loss*, Geophys. Res. Lett.,* 41, 1216–1225, doi:10.1002/2013GL05895 1.

Sugiura, K., T. Ohata, D. Yang (2006), Catch characteristics of precipitation gauges in high-latitude regions with high winds, *J. Hydromet.*, 7, 984-994.

Schweiger, A. J., R. W. Lindsay, S. Vavrus, and J. A. Francis (2008), Relationships between Arctic sea ice and clouds during autumn, *J. Climate,* 21, 4799–810.

Tjernstöm, M., and R. G. Graversen (2009), The Vertical Structure of the lower Arctic troposphere anlaysed from observations and the ERA-40 reanalysis, *Q. J. R., 133*(February), 937–948, doi:10.1002/qj.

Tjernström, M. (2005), The summer arctic boundary layer during the Arctic Ocean Experiment 2001 (AOE-2001). *Bound-Lay. Meteorol,* 117(1), 5-36.

Tjernström, M., and 43 others (2014), The arctic summer cloud ocean study (ASCOS): Overview and experimental design. *Atm. Chemistry and Physics*, 14(6), 2823-2869.

Tjernström, M., M. D. Shupe, I. M. Brooks, P. O. G. Persson, J. Prytherch, D. J. Salisbury, J. Sedlar, P. Achtert, B. J. Brooks, P. E. Johnston, G. Sotiropoulou, D. Wolfe (2015), Warm-air advection, air mass transformation and fog causes rapid ice melt, *Geophys. Res. Lett.,* 42, 5594–5602, doi:10.1002/2015GL064373.

Thompson D. W. J, and J. M. Wallace (1998), The Arctic Oscillation signature in the wintertime geopotential height and temperature fields. *Geo. Res. Lett.,* 25, 9, 1297-1300.

Tsukernik, M., D. N. Kindig, and M. C. Serreze (2007), Characteristics of winter cyclone activity in the northern North Atlantic: Insights from observations and regional modeling*, J. Geophys. Res.,* 112, D03101, doi:10.1029/2006JD007184.

Uttal, T., et al. (2002), The Surface Heat Budget of the Arctic Ocean (SHEBA), *Bull. Am. Meteorol*., 83, 255– 275.

Vaughan, D.G., J.C. Comiso, I. Allison, J. Carrasco, G. Kaser, R. Kwok, P. Mote, T. Murray, F. Paul, J. Ren, E. Rignot, O. Solomina, K. Steffen and T. Zhang, (2013) Observations: Cryosphere. In: Climate Change 2013: The Physical Science Basis. Contribution of Working Group I to the Fifth Assessment Report of the Intergovernmental Panel on Climate Change [Stocker, T.F., D. Qin, G.-K. Plattner, M. Tignor, S.K. Allen, J. Boschung, A. Nauels, Y. Xia, V. Bex and P.M. Midgley (eds.)]. Cambridge University Press, Cambridge, United Kingdom and New York, NY, USA.

Vihma, T., J. Jaagus, E. Jakobson, and T. Palo (2008), Meteorological conditions in the Arctic Ocean in spring and summer 2007 as recorded on the drifting ice station Tara, *Geophys. Res. Lett*., 35, L18706, doi:10.1029/2008GL034681.

Walden, V. P., L. Cohen, S. Y. Murphy, S. R. Hudson, M. A. Granskog (this issue) Atmospheric components of the surface energy budget over young sea ice: Results from the N-ICE2015 experiment. *J. Geophys. Res. Atmos., in review*

Walsh J. E., W. L. Chapman, D. H. Portis (2009), Arctic cloud fraction and radiative fluxes in atmospheric reanalysis, *J. Climate,* 22:2316–2334.

Wang J, Zhang J, Watanabe E, Ikeda M, Mizobata K, Walsh JE, Bai X, Wu B (2009), Is the dipole anomaly a major driver to record lows in Arctic summer sea ice extent? *Geophys. Res. Lett*., 36:L05706. doi: 10.1029/2008GL036706.

Woods, C., R. Caballero, and G. Svensson (2013), Large-scale circulation associated with moisture intrusions into the Arctic during winter. *Geophys. Res. Lett.,* 40, 4717–4721, doi:10.1002/grl.50912.

Woods, C. and R. Caballero (2016), The role of moist intrusions in winter Arctic warming and sea ice decline*, J. Climate, 29*, 4473-4485, doi: 10.1175/JCLI-D-15-0773.1.

World Meteorological Organization (2008), Guide to Meteorological Instruments and Methods of Observation, Appendix 4B, WMO-No. 8 (CIMO Guide), Geneva.

Wu B., Wang J., Walsh J.E. (2006), Dipole anomaly in the winter Arctic atmosphere and its association with sea ice motion, *J Climate,* 19:210–225.

Wyser, K., Jones, C.G., Du, P. et al. (2008), An evaluation of Arctic cloud and radiation processes during the SHEBA year: simulation results from eight Arctic regional climate models*, Clim Dyn,* 30: 203. doi:10.1007/s00382-007-0286-1

Yang, J., J. Comiso, D. Walsh, R. Krishfield, and S. Hongo (2004), Storm-driven mixing and potential impact on the Arctic Ocean*, J. Geophys. Res.,* 109, C04008, doi: 10.1029/2001JC001248.

Yang X-Y., Fyfe J.C., Flato G.M. (2010), The role of poleward energy transport in Arctic temperature evolution, *Geophys Res Lett,* 37:L14803. doi: 10.1029/2010GL042487.

Zhang, X., J. E. Walsh, J. Zhang, U. S. Bhatt, M. Ikeda (2004), Climatology and interannual variability of Arctic cyclone activity: 1948-2002. *J. Clim.,* 17, 2300-2317.

Zhang, X., A. Sorteberg, J. Zhang, R. Gerdes, J.C. Comiso (2008), Recent radical shifts of atmospheric circulations and rapid changes in Arctic climate systems. *Geophys Res Lett.* 35:L22701.

Zhang, J., R. Lindsay, M. Steele, and A. Schweiger (2008), What drove the dramatic retreat of arctic sea ice during summer 2007? *Geophys Res Lett,* 35(11), 1-5.

Zhang, J., R. Lindsay, A. Schweiger, and M. Steele (2013), The impact of an intense summer cyclone on 2012 Arctic sea ice retreat, *Geophys. Res. Lett.,* 40, 720-726, doi: 10.1002/grl.50190.

Table 1 Summary of instrumentation used to collect meteorological data during N-ICE2015.

	Physical Parameters	Instrument	Instrument Accuracy[1]	Dates of operation
Supersite	Air temperature & Relative humidity 2, 4, and 10 meters a.g.l.	Vaisala HMP155 with RM Young Model 43502 with ventilated radiation shield	± 0.3˚C ± 2.4%	2m: Floes 1, 2, 3 & 4 4m: Floes 1,2, partial 3 (31 May—6 Jun), 4 10m: Floe 1, 2, partial 3 (1 May—6 Jun), 4
Supersite	Wind speed and direction 2, 4, and 10 meters a.g.l.	Lufft Ventus V200A-UMB (2D ultrasonic)	± 0.2 m s^{-1} and < 2˚ RMSE (for windspeeds > 1 m s^{-1})	2m: Floes 1 (intermittent), 2, 3, 4 4m: Floes 1 (intermittent), 2, 3 10m: Floes 1 (intermittent), 2, 3, 4
Supersite	Surface Pressure	RM Young 61302V	± 0.3 hPa	Floes 1-4
Supersite	Precipitation (water equivalent)	Tretyakov shielded gauge	Up to 50% undercatch during high winds[2]	Floes 1-3
Ship-based	Vertical profiles of temperature, humidty, & winds	Vaisala RS92 SGP radiosondes with MW31 ground station	P: 1 hPa T: 0.5˚C RH: 5% WS: 0.15 m s^{-1} WD: 2˚	Twice daily: 16 Jan—26 Mar 17 Apr—22 Jun
Ship-based	Air pressure at ~22 m agl	Aanderaa pressure sensor 2810	~1 hPa lower than Supersite pressure sensor[3]	Floes 1-4 & transitions: 19 Jan*—18 Feb 23 Feb—19 Mar 18 Apr—5 Jun 7 Jun—19 Jun *wind speed measurements started on 22 Jan
Ship-based	Air temperature at ~22 m agl	Aanderaa temperature sensor 3455, shielded (not ventilated)	< 1˚C difference from 2 m temperature during well-mixed conditions[3]	
Ship-based	Wind speed & direction at ~24m agl	Thies Clima 2D ultrasonic	± 0.1 m s^{-1} and ± 1˚ For reconstructed 10 m WS[3], RMSE = 0.58 m/s	

[1] Based on instrument specifications.
[2] Goodison et al., 1998
[3] Based on comparison of all concurrent measurements between ship-based sensor and Supersite sensor.

Table 2 Summary of N-ICE2015 storm events.

	Storm	Winds			Pressure[4]		Temperature[4]	
	M: major storm[1] m: minor storm	Strong wind periods (wind speeds > 8 m/s)[2] Start	End	Peak wind speed[3]	Maximum rate of decrease	Minimum	Minimum	Maximum
		(UTC)		(m/s)	(hPa/ 6 hr)	(hPa)	(˚C)	(˚C)
Winter	**M1**	21-Jan, 21:00[+]	22-Jan, 07:00	10.8	9	990	-27.4	-3.1
	M2	3-Feb, 11:00	8-Feb, 21:00	22.0	14	967	-35.5	-1.4
	m1	13-Feb, 04:00	13-Feb, 09:00	10.0	1	989	-36.4	-26.0
	M3[**]	15-Feb, 12:00	16-Feb, 17:00	22.5	16	976	-34.1	-0.2
		17-Feb, 16:00	21-Feb, 04:00*	11.9				
	m2	22-Feb, 08:00*	23-Feb, 01:00*	10.3*	4*	980*	-32.3*	-20.9*
	m3	25-Feb, 06:00*	25-Feb, 20:00*	8.7*	4*	1001*	-29.1*	-15.5*
	M4	2-Mar, 10:00	4-Mar, 01:00	16.8	5	998	-25.6	-3.1
	M5	7-Mar, 08:00	8-Mar, 18:00	14.2	5	966	-19.5	-1.9
	M6	14-Mar, 21:00	16-Mar, 23:00*	19.2	21	966	-31.3	-2.2
Spring	**m4**	23-Apr, 10:00*	24-Apr, 12:00*	14.3*	1*	1009*	-22.9*	-14.3*
	M7	25-Apr, 04:00	27-Apr, 23:00	12.6	5	1021	-20.3	-9.7
	m5[**]	6-May, 23:00	8-May, 02:00	10.0	3	1012	-17.3	-13.3
		9-May, 16:00	10-May, 19:00	10.4				
	m6	16-May, 12:00	16-May, 23:00	12.3	4	1003	-15.0	0.3
	m7	21-May, 10:00	23-May, 01:00	15.4	3	1004	-13.5	-9.0
	m8	29-May, 17:00	30-May, 05:00	10.6	3	1012	-4.9	-2.2
	M8	2-Jun, 15:00	6-Jun, 13:00*	13.7	5	1003	-3.0	+0.5
	m9	8-Jun, 1:00	8-Jun, 6:00	12.0	2	1000	+0.2	+1.5
	m10	11-Jun, 2:00	14-Jun, 5:00	17.3	4	1002	-2.9	+0.7

[1] Major/minor designation is based on the maximum rate of pressure decrease: 'Major' storms (M) are > 5 hPa per 6 hours; 'minor' storms (m) are < 5 hPa per 6 hours.

[2] Start and end dates/times correspond to periods when the 10-minute averaged wind speed (at 10 meters) was greater than **8 m/s** lasting more than 3 hours, with no breaks more than 1 hour long. Times are to the nearest hour.

[3] From 1-minute data

[4] Pressure & temperatures are determined from the period 1 day before and after the high-wind start/end times.

* Values are from shipboard instruments (meteorological tower data not available).

[**] Storms have two separate periods of high winds.

[+] No wind data before this time--start date/time unknown.

Figure 1 Location and start/end dates of N-ICE2015 drifts. Approximate location of sea ice edge for Jan-Jun 2015 shown as dashed line (from NSIDC monthly mean sea ice extent *https://nsidc.org/data/seaice_index/*).

Figure 2 a) Aerial photo of N-ICE2015 Floe 3 showing Supersite location relative to the ship; **b)** meteorological tower in January. Temperature and relative humidity sensors in aspirated housings and wind speed and direction sensors (on horizontal arms for lowest 2 levels) are located at 2, 4, and 10 m above snow surface. (Aerial photo courtesy of Vasily Kustov and Sergey Semenov, Arctic and Antarctic Research Institute, St. Petersburg, Russia.)

Figure 3 Time series of near-surface meteorological parameters during N-ICE2015: **a)** surface pressure, **b)** temperature (2 m), **c)** relative humidity with respect to ice (2 m), and **d)** wind speed and direction (10 m). The four floes are delineated and gaps in data are when the ship was moved to a new floe. Wind direction is indicated by color as the compass direction that wind is coming from. Temperature and pressure data that has been filled from ship-based measurements are noted by grey lines; wind speeds filled from ship-based measurements are noted by grey bars on the x-axis.

Figure 4 Wind speed and direction distributions (from 1-minute data) for **a)** winter (JFM) and **b)** spring/summer (AMJ). Note differences in frequency scales.

Figure 5 Probability distribution functions for measured meteorological variables for **a-d)** winter (JFM) and **e-h)** spring/summer (AMJ). Bin sizes for sea level pressure is 5 hPa , 2m temperature is 2˚C, 10m wind speed is 1 ms^{-1}, and relative humidity wrt. ice is 5%. Black lines are N-ICE2015 observations, dashed line is the mean climatology from ERA-I (1979-2015). Shaded area indicates the range of all ERA-I distributions.

Figure 6 Winter (JFM) 2015 **a)** 500 hPa GPH mean (contours) and anomaly (shading), **b)** near-surface (925 hPa) temperature anomaly, and **c)** near-surface (925 hPa) wind vector anomaly and geopotential height anomaly: **d-f)** same as for a-c, but for spring/summer (AMJ) 2015. Data from NCEP Reanalysis dataset (*NOAA-ESRL Physical Sciences Division, www.esrl.noaa.gov/psd/).* Anomalies are derived as differences from the 1981-2010 climatology. GPH units are meters, temperature anomaly units are K, wind vector units m s^{-1}.

Figure 7 Monthly mean Arctic Oscillation (AO) and North Atlantic Oscillation (NAO) indices for December 2014 through July 2015. Data from NOAA CPC daily AO and NAO indices (http://www.cpc.ncep.noaa.gov/).

Figure 8 a) June 2015 mean sea level pressure (hPa), **b)** surface air temperature anomaly (K), and **c)** near-surface (925 hPa) meridional wind anomaly (m s^{-1}) (+ is southerly, - is northerly). Yellow arrows

in wind anomaly plots indicate wind directions. Data from NCEP Reanalysis dataset (*NOAA-ESRL Physical Sciences Division, www.esrl.noaa.gov/psd/).*

Figure 9 Synoptic situation for each of the 6 Major winter storms from NOAA-GFS. Contours are SLP (5 hPa intervals) and colors are surface temperature. The map state shown is the nearest (12-hourly) to when the lowest pressure occurred at the N-ICE2015 site (marked with black X). Black dots indicate the approximate center of the low pressure at daily intervals during the N-ICE2015 storm period and for 4 days prior.

Figure 10 a) Synoptic situation for spring storm M8 and **b)** m6 from NOAA-GFS. Contours are SLP (5 hPa intervals) and colors are surface temperature. The map state shown is the nearest (12-hourly) to when the lowest pressure occurred at the N-ICE2015 site (marked with black X). Black dots indicate the approximate center of the low pressure at daily intervals during the N-ICE2015-defined storm period and for 4 days prior.

Figure 11 Mean temperature profiles to 5 km agl during winter (19 Jan to 20 Mar) for **a)** radiatively clear state (netLW < - 30 W m^{-2}) and **b)** opaquely cloudy state (netLW > -10 W m^{-2}). Black lines are N-ICE2015, grey lines are SHEBA profiles. Dashed lines are ±1 standard deviation.

Figure 12 Weekly averaged temperature profiles for weeks 16-25 (14 April—22 June). Each profile is the mean of ~14 profiles. Note lifted temperature inversions in nearly all of the profiles.

Figure 13 Radiosonde profiles from 6 May, launched at ~23h UTC, showing **a)** temperature, **b)** relative humidity, and **c)** specific humidity. Grey bars show two collocated temperature and specific humidity inversions which correspond to the upper portion of super-saturated (RH_i > 100%) layers (ie. where clouds are likely).

Figure 1.

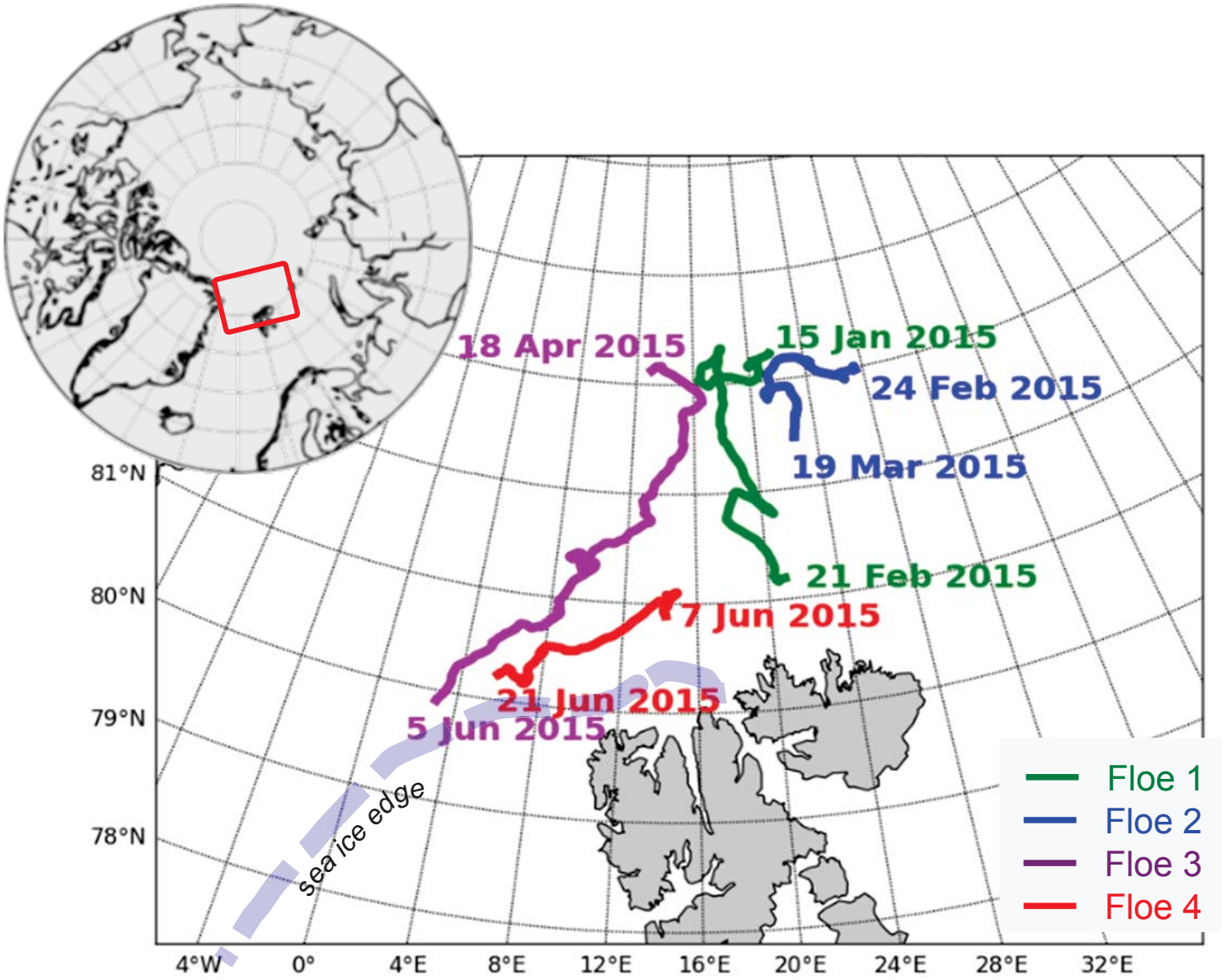
18 Apr 2015
15 Jan 2015
24 Feb 2015
19 Mar 2015
21 Feb 2015
7 Jun 2015
21 Jun 2015
5 Jun 2015
sea ice edge
81°N
80°N
79°N
78°N
4°W
0°
4°E
8°E
12°E
16°E
20°E
24°E
28°E
32°E
Floe 1
Floe 2
Floe 3
Floe 4

Figure 2.

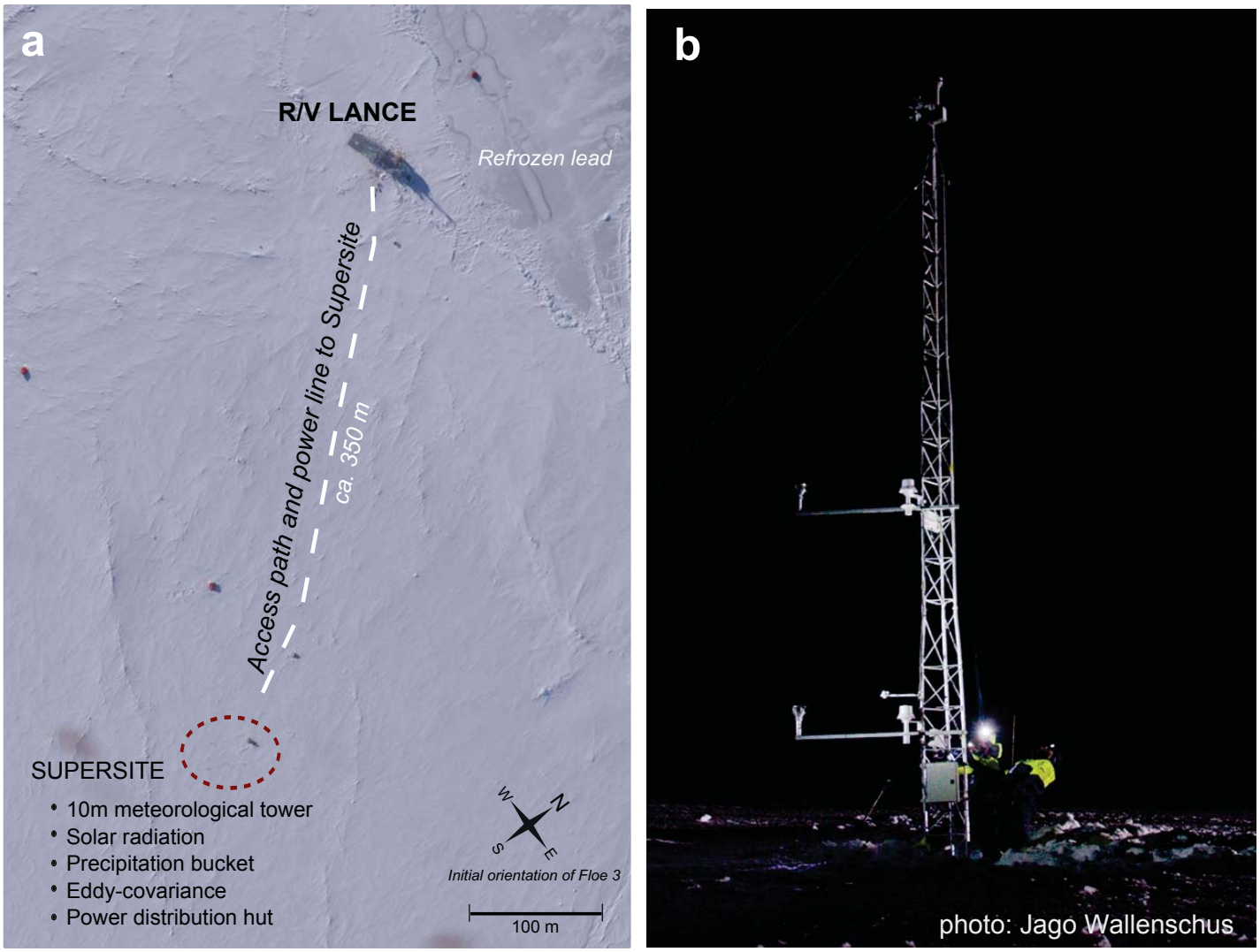
a
R/V LANCE
Refrozen lead
Access path and power line to Supersite
ca. 350 m
SUPERSITE
• 10m meteorological tower
• Solar radiation
• Precipitation bucket
• Eddy-covariance
• Power distribution hut
W
N
S
E
Initial orientation of Floe 3
100 m
b
photo: Jago Wallenschus

Figure 3.

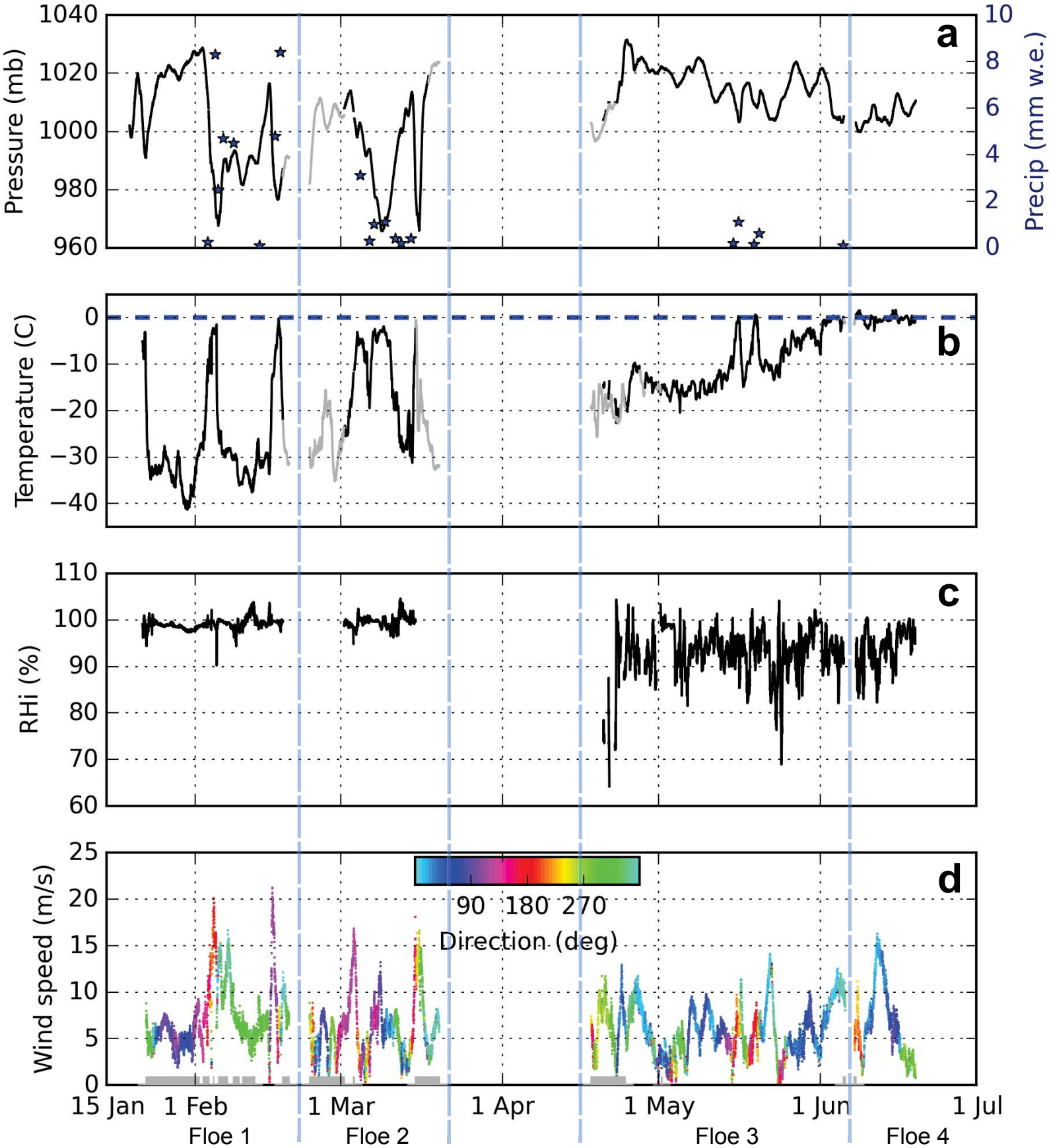
a
Pressure (mb)
Precip (mm w.e.)
1040
1020
1000
980
960
10
8
6
4
2
0
b
Temperature (C)
0
−10
−20
−30
−40
c
RHi (%)
110
100
90
80
70
60
d
Wind speed (m/s)
25
20
15
10
5
0
90 180 270
Direction (deg)
15 Jan
1 Feb
1 Mar
1 Apr
1 May
1 Jun
1 Jul
Floe 1
Floe 2
Floe 3
Floe 4

Figure 4.

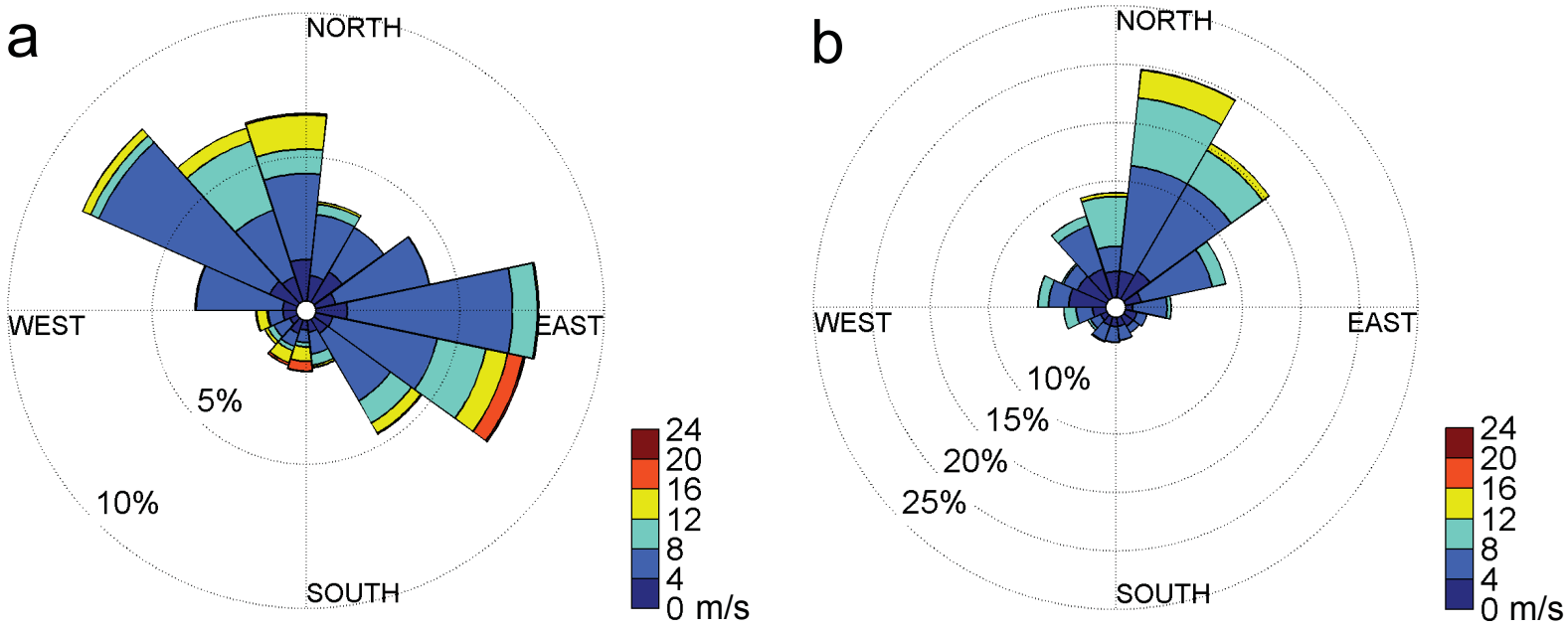
a
NORTH
WEST
EAST
SOUTH
5%
10%
24
20
16
12
8
4
0 m/s
b
NORTH
WEST
EAST
SOUTH
10%
15%
20%
25%
24
20
16
12
8
4
0 m/s

Figure 5.

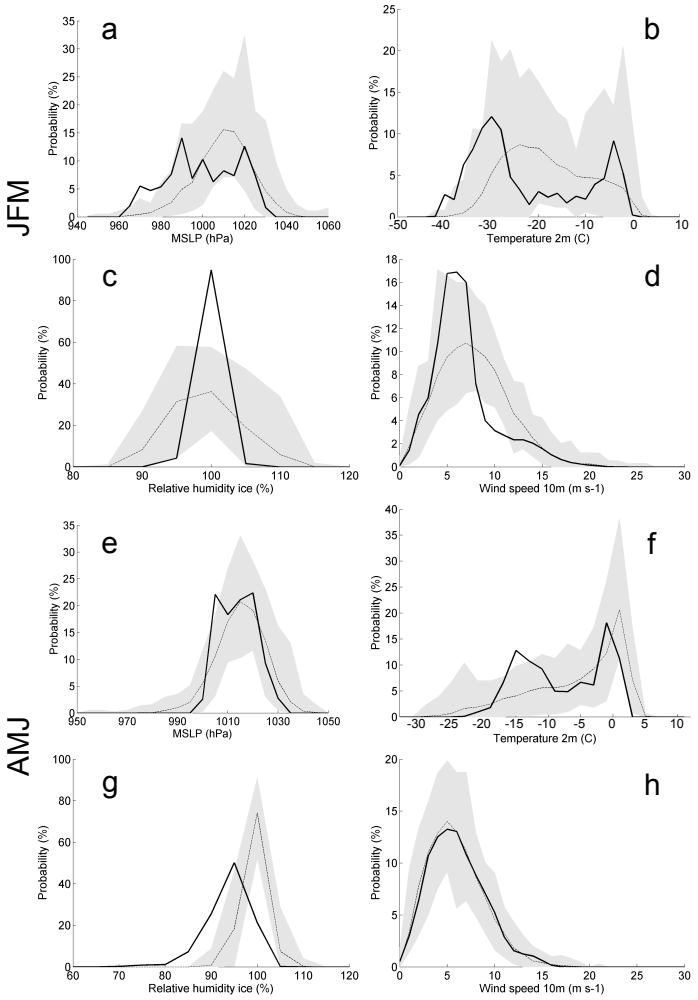
JFM
AMJ
a
b
c
d
e
f
g
h
Probability (%)
MSLP (hPa)
Temperature 2m (C)
Relative humidity ice (%)
Wind speed 10m (m s-1)

Figure 6.

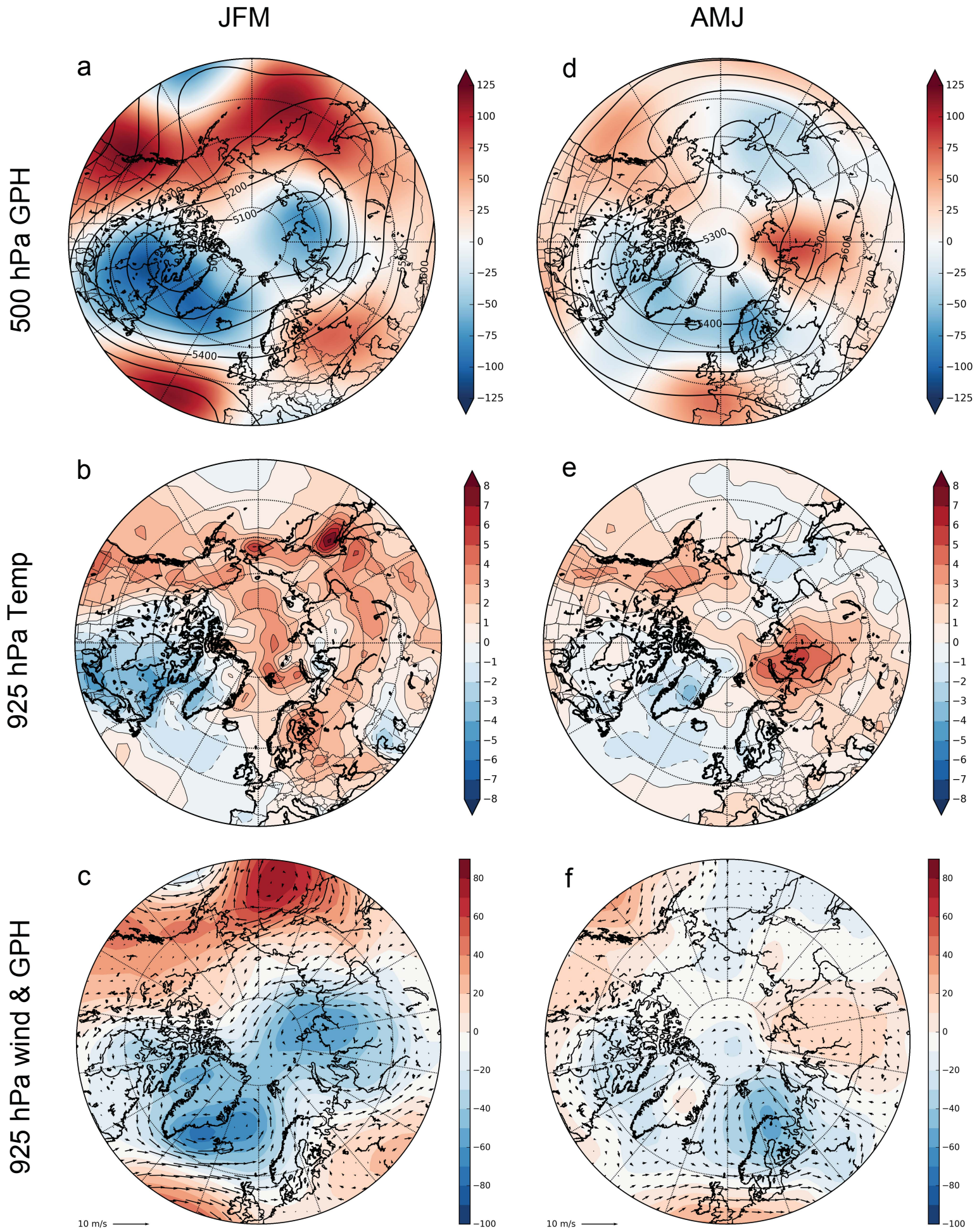
JFM
AMJ
500 hPa GPH
925 hPa Temp
925 hPa wind & GPH
a
b
c
d
e
f
5400
5300
10 m/s

Figure 7.

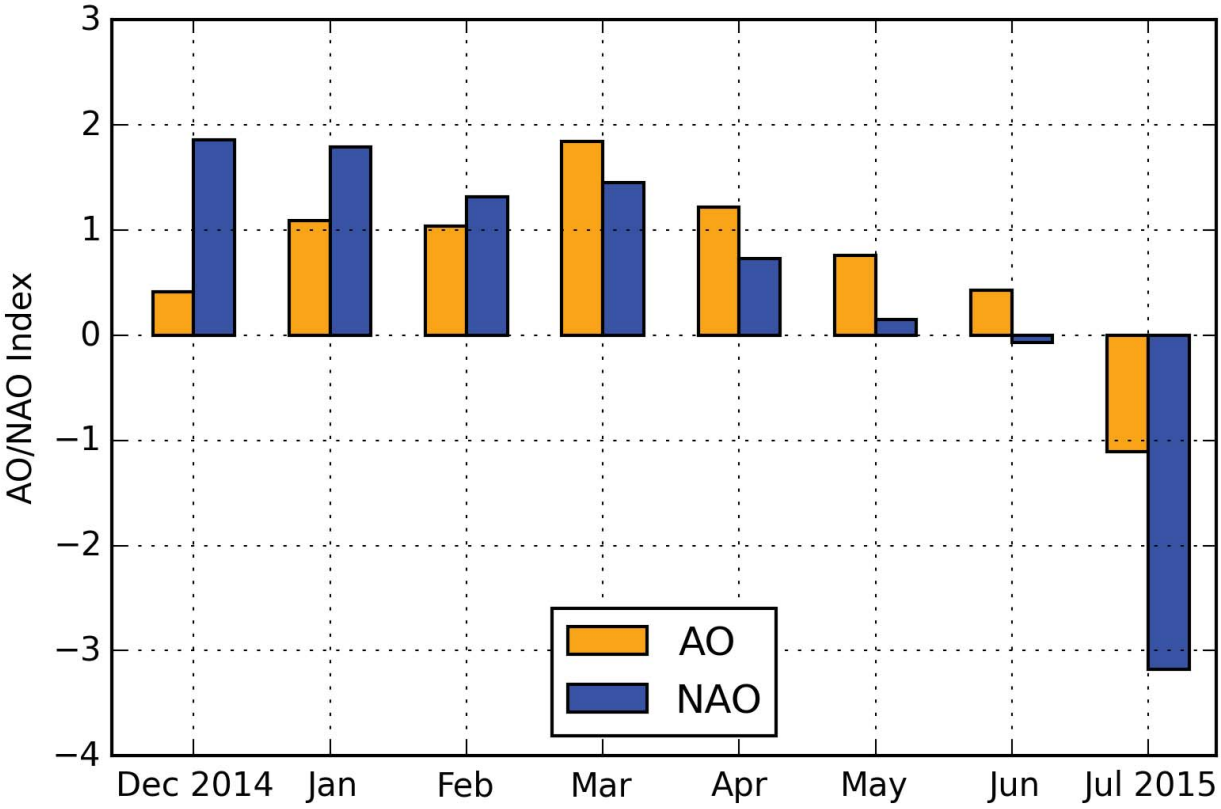
3
2
1
0
−1
−2
−3
−4
AO/NAO Index
Dec 2014
Jan
Feb
Mar
Apr
May
Jun
Jul 2015
AO
NAO

Figure 8.

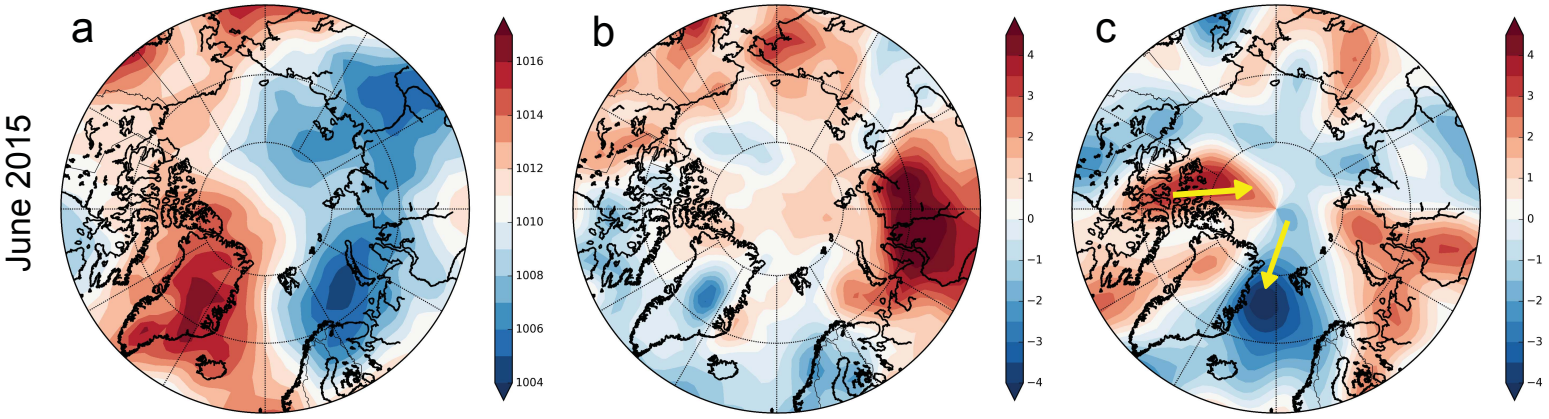
June 2015
a
1016
1014
1012
1010
1008
1006
1004
b
4
3
2
1
0
−1
−2
−3
−4
c
4
3
2
1
0
−1
−2
−3
−4

Figure 9.

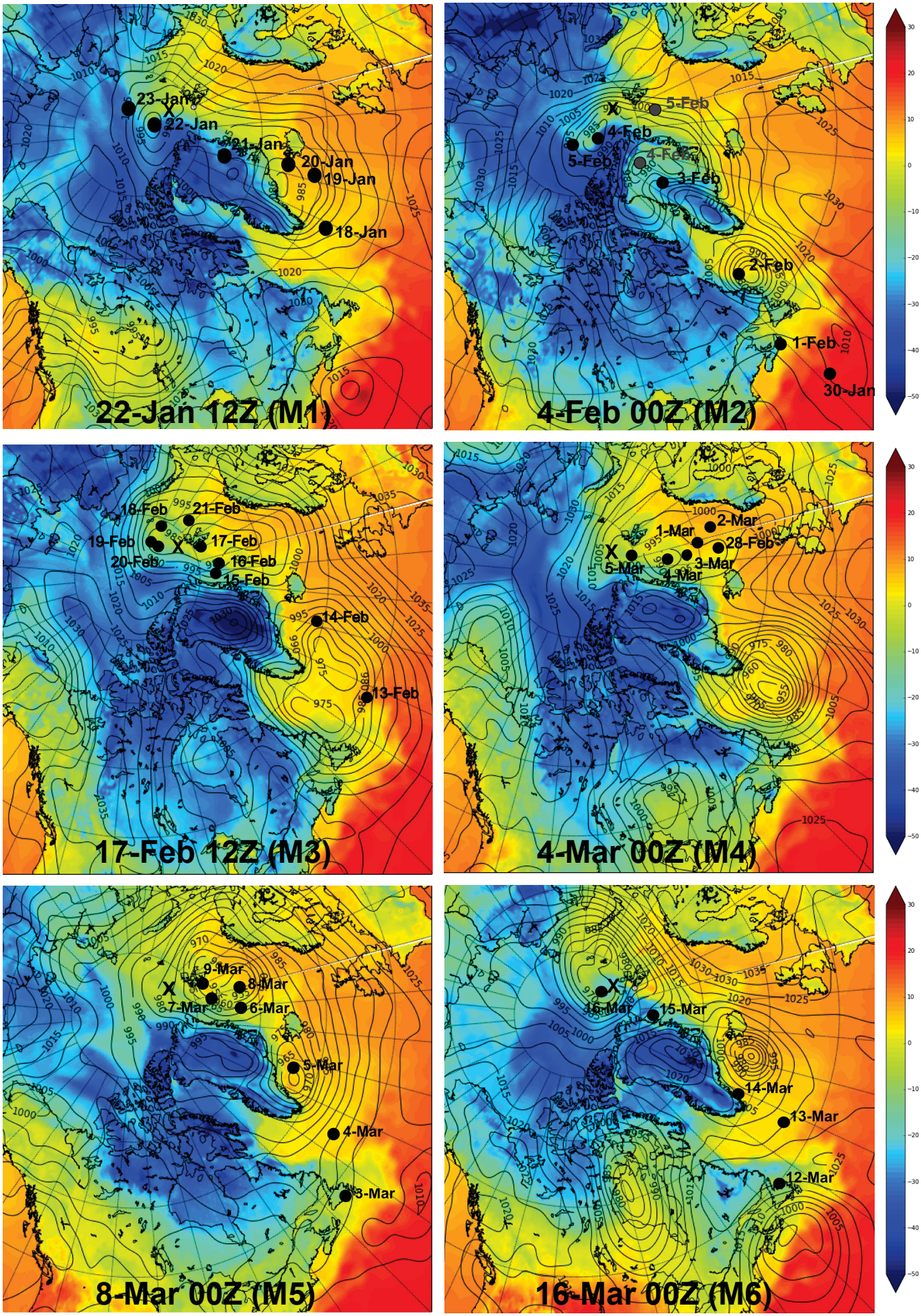
23-Jan
22-Jan
21-Jan
20-Jan
19-Jan
18-Jan
22-Jan 12Z (M1)
5-Feb
4-Feb
5-Feb
4-Feb
3-Feb
2-Feb
1-Feb
30-Jan
4-Feb 00Z (M2)
18-Feb
21-Feb
19-Feb
17-Feb
20-Feb
16-Feb
15-Feb
14-Feb
13-Feb
17-Feb 12Z (M3)
2-Mar
1-Mar
28-Feb
5-Mar
3-Mar
4-Mar
4-Mar 00Z (M4)
9-Mar
8-Mar
7-Mar
6-Mar
5-Mar
4-Mar
3-Mar
8-Mar 00Z (M5)
16-Mar
15-Mar
14-Mar
13-Mar
12-Mar
16-Mar 00Z (M6)

Figure 10.

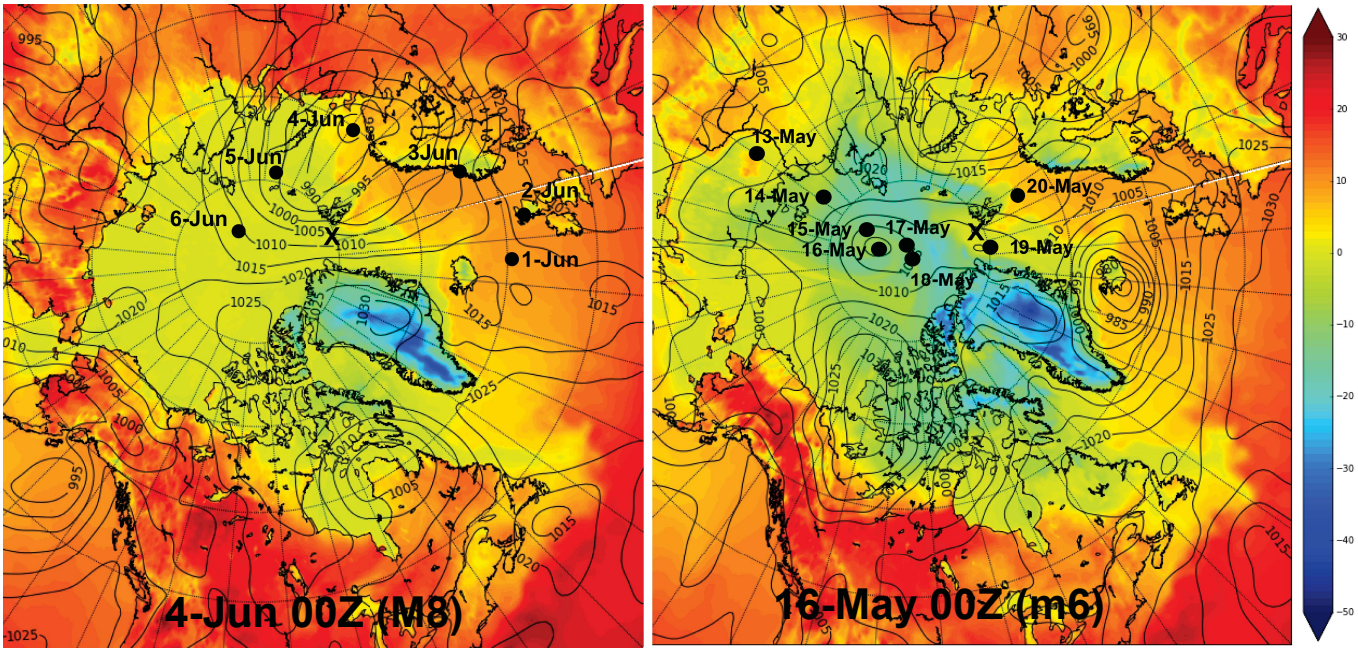
4-Jun
5-Jun
3Jun
2-Jun
6-Jun
1-Jun
4-Jun 00Z (M8)
13-May
14-May
15-May
16-May
17-May
18-May
19-May
20-May
16-May 00Z (m6)

Figure 11.

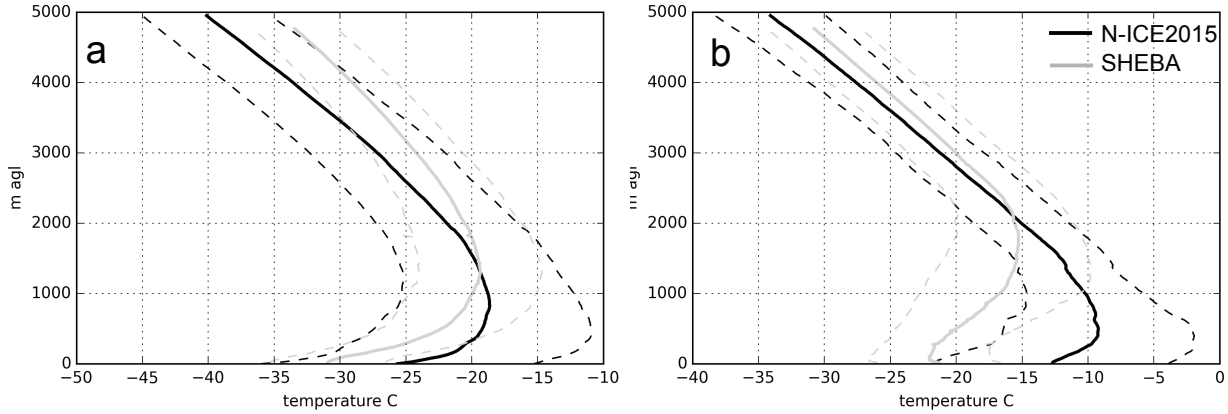
a
b
N-ICE2015
SHEBA
m agl
temperature C
5000
4000
3000
2000
1000
0
−50
−45
−40
−35
−30
−25
−20
−15
−10
−5

Figure 12.

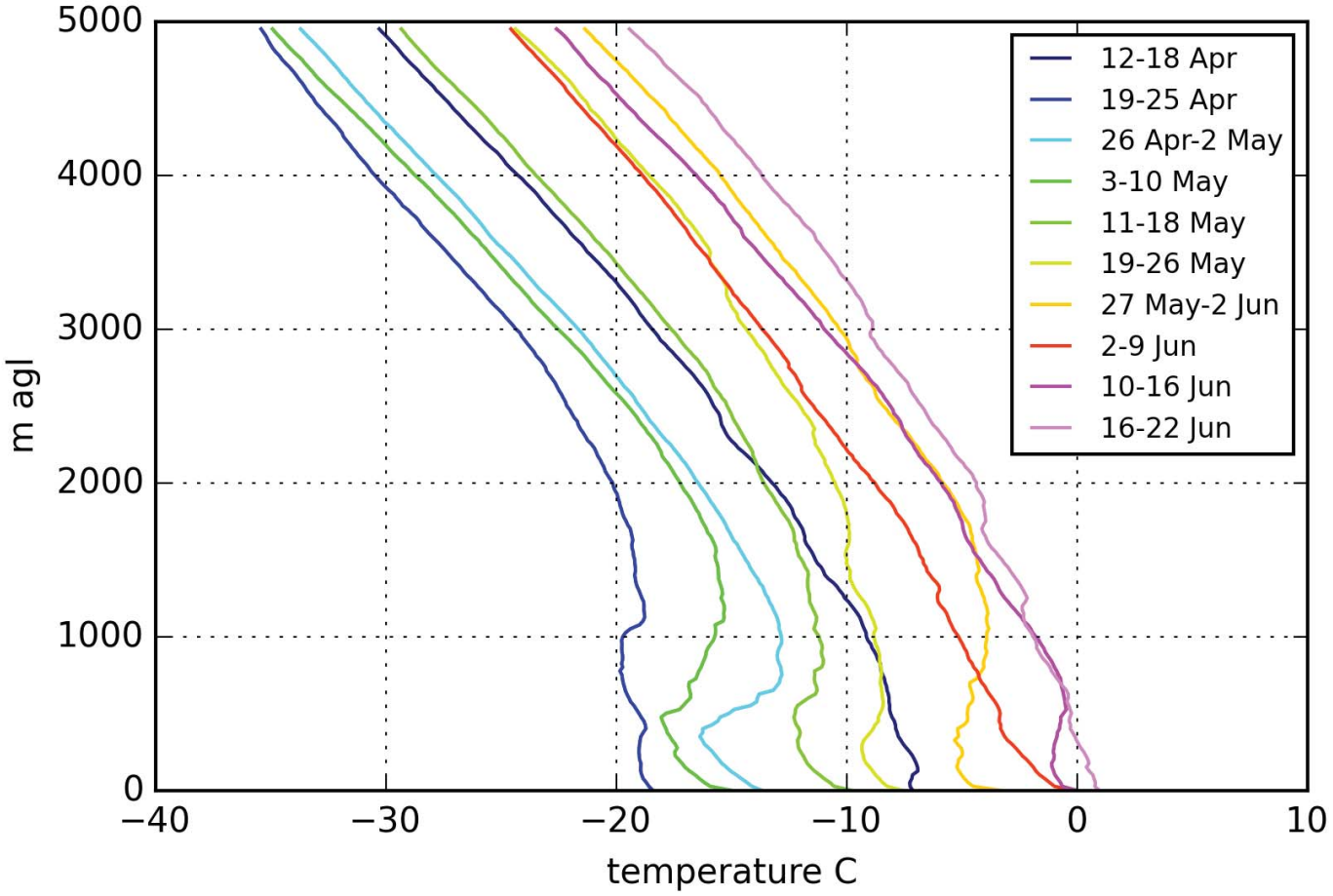
5000
4000
3000
2000
1000
0
m agl
−40
−30
−20
−10
0
10
temperature C
12-18 Apr
19-25 Apr
26 Apr-2 May
3-10 May
11-18 May
19-26 May
27 May-2 Jun
2-9 Jun
10-16 Jun
16-22 Jun

Figure 13.

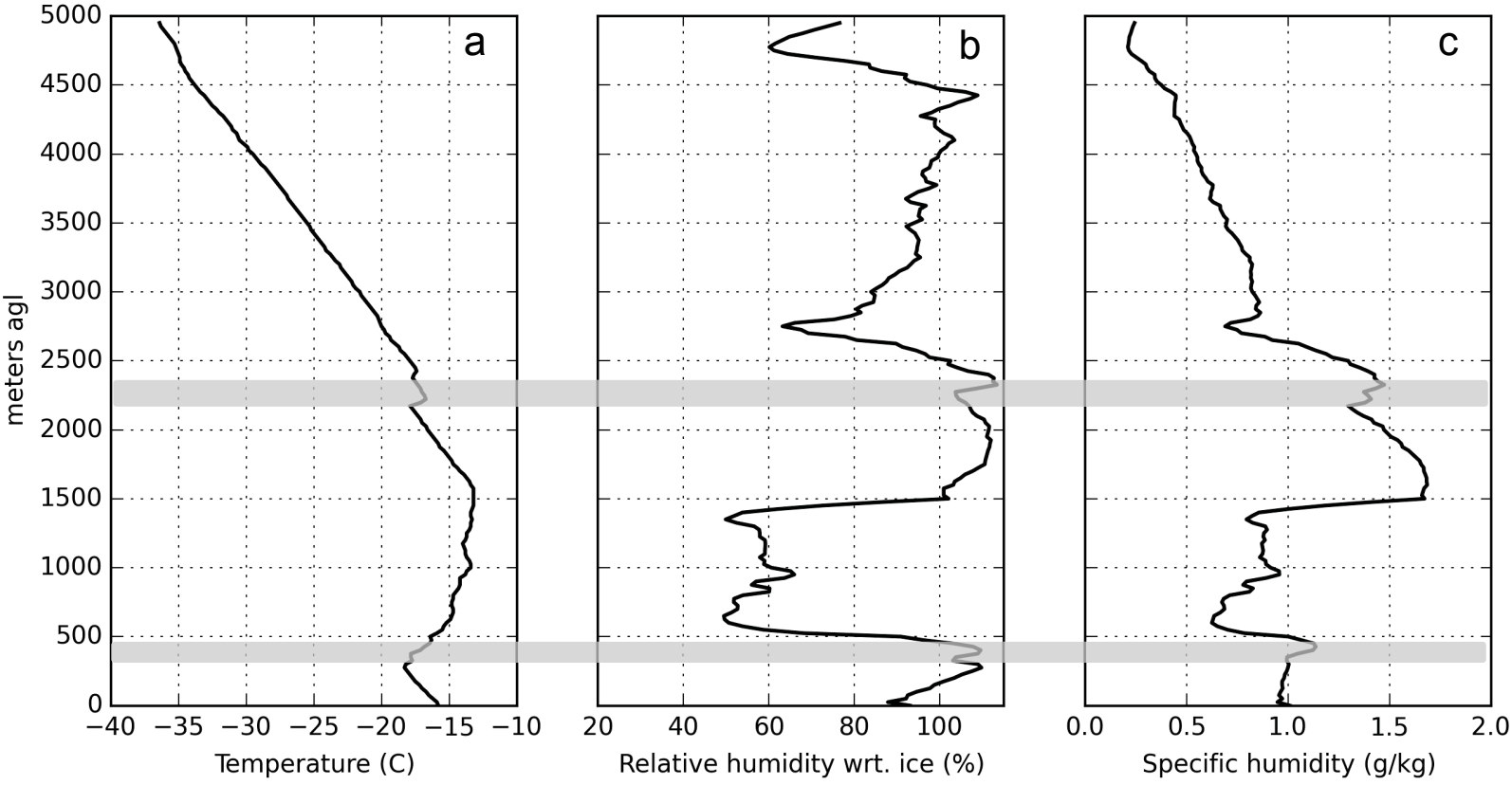
a
b
c
meters agl
5000
4500
4000
3500
3000
2500
2000
1500
1000
500
0
−40 −35 −30 −25 −20 −15 −10
Temperature (C)
20 40 60 80 100
Relative humidity wrt. ice (%)
0.0 0.5 1.0 1.5 2.0
Specific humidity (g/kg)